AERE - R 10258

United Kingdom Atomic Energy Authority

HARWELL

Quantitative Acoustic Emission for Source Characterization in Metals

H.N.G. Wadley, C.B. Scruby, J.E. Sinclair, K. Rusbridge
and J.A. Hudson
Materials Physics, Metallurgy and Theoretical Physics Divisions
AERE Harwell, Oxfordshire

October 1981

AERE - R 10258

QUANTITATIVE ACOUSTIC EMISSION FOR SOURCE CHARACTERIZATION IN METALS

by

H.N.G. Wadley, C.B. Scruby, J.E. Sinclair, K. Rusbridge, J.A. Hudson

ABSTRACT

There are two problems limiting the application of acoustic emission to structural integrity evaluation in metals. These are a variability in the emission 'activity' of different metals and an inability to characterize detected and located sources. In an approach to understanding the first problem we have studied the acoustic emission generated during deformation of specially prepared Al 5.4% Zn 2.5% Mg in a series of systematically varied heat treated conditions. It was found that the development of intense localized slip in peak aged material was the dominant emission source. A quantitative approach to the second (source characterization) problem is reviewed and then extended by presentation of recent results from an investigation into the effects of a nearby precrack upon the emission from cleavage microcracking. It is shown that source characterization is made somewhat more difficult; but the most important effect of the precrack is its action as an amplifier, making the source appear apparently $\sim$10 times stronger.

Materials Physics, Metallurgy and Theoretical Physics Divisions,
AERE Harwell

October 1981

HL81/3019 (C14)

CONTENTS

TABLES

Table

ILLUSTRATIONS

Fig.

ILLUSTRATIONS (cont'd)

Fig.

16 Applied load and acoustic emission amplitude as a function of crosshead displacement for CTS specimen SW 602

17(a) Four typical emissions recorded at Epicentre (1) from crack-growth in specimen SW 600

17(b) Four typical emissions recorded at Epicentre (2) from crack-growth in specimen SW 602

18 Showing source strength derived as a function of time by deconvolution of the ½-space Green's function from acoustic emissions detected at both Epicentres

19(a) Histograms of source strength (volume) data for all the emissions recorded at each Epicentre

19(b) Histograms of source lifetime data for all the emissions recorded at each Epicentre

20 Microcrack is modelled as edge dislocation loop, which is equivalent to combination of 3 force dipoles, D_{11}

21 Displacement waveforms computed, assuming ½-space solution, for two Epicentres of CTS specimen in response to microcrack source at crack tip

22 Simplified model for crack grown

23 Source volume (per unit thickness) as function of time, based on model in Fig. 24

1. Introduction

Harwell, the Admiralty Marine Technology Establishment (Holton Heath) and the Royal Aircraft Establishment (Farnborough) have been jointly studying basic aspects of the acoustic emission of metals. The programme has been concerned with two problems:

- From what processes is acoustic emission generaged during the deformation and fracture of metals? This area is concerned with understanding why some metals emit much detectable acoustic emission whilst others emit almost none. It is thus concerned with the RELIABILITY of the acoustic emission technique for nondestructive evaluation (NDE) applications.
- How do you determine the significance, in terms of impact upon structural integrity, of a detected AE signal? This area is therefore concerned with quantitative methods of source CHARACTERIZATION.

This paper presents a few of the results obtained from recent studies in each of the two areas.

2. The Origin of Acoustic Emission Signals

2.1 Introduction

The high strength 7075 series of aluminum alloys are finding increasing uses in aerospace structures, and there is a growing interest in the potential use of acoustic emission techniques to detect and monitor flaw growth in such structures[1]. With funding from RAE, Harwell has been pursuing a basic study to ellucidate the origin of detectable acoustic emission signals in this alloy system.

It is recognized that the defect to be detected in practice will be the initiation/propagation of a fatigue crack in peak (or overaged) material. However, plastic deformation processes are the precursor to the crack nucleation

event and such processes also occur in the plastic zone expanding from the fatigue crack tip. Consequently, the first stage of the project is determination of the emission characteristics of deformation processes.

These deformation processes are strongly influenced by microstructure[2] e.g. grain size, precipitate type and distribution etc., and the project was designed to use this to help determine the emission mechanism. It would also provide useful data on the sensitivity of the acoustic emission generation to metallurgical variables.

2.2 Experimental

2.2.1 Materials

Since metallurgical variables have a strong influence upon deformation behavior and since commercial materials have a complex microstructure containing impurities and a range of intermetallic inclusions it was decided to perform experiments upon a pure form of 7075 aluminum.

A 5½" diameter casting was prepared by melting an appropriate composition charge, adding a Foseco 190 degassing pellet and then pouring at ∿700°C into a chilled mold. The melt was directionally solidified at a rate of 3½" min^{-1}. Chemical analysis was made of material from the top and bottom of the casting and the results of this are shown in table 1.

TABLE 1 Bulk Chemical Composition of Al Zn Mg alloy, F68

		Zn	Mg	Cu	Zr	Fe	Al
ALLOY F68	Top	5.49	2.41	-	-	<0.02	Balance
	Bottom	5.60	2.48	-	-	<0.02	Balance
NB. Other elements below detection limit							

These analyses indicate negligable macrosegregation. After casting the ingot was given a homogenising heat treatment of 24h at 450°C. It was then rolled to 60mm thick plate. Samples for microsegregation studies were taken at this point and these indicated that after a solution treatment of 2h at 465°C, only minor Zn and Mg microsegregation was present, their compositions varying by no more than 20% over distances of ∿500μm. The material was, as far as could be ascertained from optical metallography, virtually inclusion free.

2.2.2 Sample Geometry and Heat Treatment

Cylindrical geometry tensile samples were cut from the plates. Their dimensions are shown in Fig. 1. The advantage of this geometry was that a gripping arrangement, during mechanical testing, could be designed to allow a transducer to be attached for acoustic emission measurements, with its axis of polarization aligned with the tensile axis of the sample, simplifying, somewhat, the interpretation of the data.

The samples were all solution treated at 465°C for 2h and then pairs of samples given one of three isothermal aging treatments: Natural aging at room temperature, 120°C single aging or 120°C for 24h followed by a second isothermal aging at 180°C. One sample of each condition was used for mechanical properties measurements, the other was used for acoustic emission measurements.

2.2.3 Mechanical Properties

Specimens were tested on a 50kN universal servo-hydraulic testing machine with full autographic recording equipment and a computerized data acquisition system. Sample extension was measured by means of a clip-on extensometer to an accuracy of ±0.2%. All the tests were carried out under ram displacement control and the ram speed was adjusted to be approximately that of the acoustic emission tests, $10^{-4}s^{-1}$.

Load vs extension curves were plotted throughout each test. Additionally, the load was digitally recorded with 10 bit precision and the digitally recorded

test data analyzed to give reference mechanical properties.

2.2.4 Narrow Band Acoustic Emission Measurements

The objective here was to deform samples under controlled mechanical conditions and to measure a standard parameter of the acoustic emission response that could then be used to measure acoustic emission activity. The effect of heat treatment upon this activity could then be systematically investigated. No attempt, in this type of approach, at source characterization was made.

For this type of experiment we have preferred the use of a broad band piezoelectric transducer whose bandwidth covered a significant portion of the acoustic emission spectrum and to measure the acoustic emission power. This approach has the following advantages:

- the result is less dependent upon changes of background noise level compared with counting techniques.
- the major specimen resonances (the frequencies at which most energy propagates) are more likely to be covered by the system bandwidth making changes in source spectrum less likely to alter the observed emission response.

A bandpass of 0.1 to 1.0MHz was chosen as the best compromise between optimum signal to noise ratio and wide bandwidth. To achieve this a 2.5MHz, heavily damped transducer, manufactured from PZT5A, was used. The electrically insulating shoe commonly incorporated into commercial transducers (to reduce ground loop pick-up) was excluded to improve sensitivity. To reduce ground loop noise, the grips contained electrical insulators thus isolating the transducer, Fig. 2.

The transducer was coupled to the specimen with Dow-Corning grease and held in position with a small spring. Since we measure acoustic power which is related to (particle velocity)^2 the transducer output was passed to a preamplifier that both differentiated and amplified the signal. This then gave a voltage that was approximately proportional to velocity. The transfer function of the preamplifier, at 1MHz, was $2.5 \times 10^5 VA^{-1}$. The signal was bandpass filtered at 0.1 and 1.0MHz, further amplified 58dB and its power measured using a Hewlett-Packard 435A power

meter. It was estimated that the smallest detectable displacement, within the system bandpass, that could be detected was $\sim 10^{-14}$m. The transfer function for signals of larger displacement was too complex to allow source characterization.

2.3 Results

2.3.1 Mechanical Properties

Mechanical properties data for this alloy are summarized in table 2. Natural aging caused an increase in 0.1% proof and ultimate tensile stresses, a slight loss of ductility, little change in workhardening rate and a small decrease in the workhardening exponent (n) of the relation.

$$\sigma_T = k\varepsilon_T^n$$

where σ_T is the true stress and ε_T the true plastic strain.

Aging for up to 59,000 minutes at 120°C caused the alloy to age harden, peak hardness occurring after ~6,000 minutes aging. This was accompanied by a loss of ductility, an increase in work hardening rate at small plastic strains and a decrease in work hardening exponent for plastic strains of 5% or more.

Aging, at 180°C, samples previously aged 24h at 120°C (double aging) resulted in a loss of strength, partial restoration of ductility, reduction in the small strain work hardening rate but little effected the work hardening exponent.

2.3.2 Microstructure

Solution treating at 465°C resulted in an equiaxed grain structure with an average grain size of 420μm. Using transmission electron microscopy we were unable to resolve any precipitation during natural aging. However, significant hardening was observed following heat treatment and Kovacs et al[3] have attributed this to the formation of solute rich GP zones. Using X-ray methods they found the zones were ~1nm in diameter after 1d and ~1.5nm after 7 days room temperature aging. We first observed precipitation in samples aged at 120°C for 24h. These were spherical in shape and ~4nm in diameter, Fig 3(a). The precitate density was $\sim 2 \times 10^{17}$cm^{-3}. Whilst grain interior precipitation appeared

TABLE 2

MECHANICAL PROPERTIES OF Al 5.5% Zn 2.5% Mg ALLOY

HEAT TREATMENT	STRESS/MPa			UNIFORM* STRAIN	WORKHARDENING RATE/GPa			WORKHARDENING EXPONENT		
	$\sigma_{0.1}$	$\sigma_{0.2}$	σ_{UTS}		ε=.001	ε=.01	ε=.05	ε=.001	ε=.01	ε=.05
ISOCHRONAL AGEING AT 20°C										
Quenched	80	84	218	0.184	4.4	1.6	1.2	0.05	0.11	0.41
1d	100	103	243	0.183	9.0	0.9	1.3	0.08	0.05	0.36
7d	172	179	301	0.127	9.9	3.0	1.1	0.06	0.10	0.22
30d	306	213	336	0.120	9.6	3.4	1.3	0.05	0.08	0.20
ISOCHRONAL AGEING AT 120°C										
Quenched	80	84	218	0.184	4.4	1.6	1.2	0.05	0.11	0.41
6 min	115	121	241	0.126	7.7	2.1	1.3	0.06	0.11	0.32
12	139	146	270	0.165	10.6	2.2	1.2	0.08	0.09	0.27
24	140	148	247	0.125	7.7	2.6	1.0	0.05	0.10	0.21
36	177	187	294	0.113	10.9	2.9	1.2	0.06	0.09	0.20
60	140	153	258	0.089	14.1	3.0	1.2	0.11	0.12	0.24
120	232	242	329	0.086	13.5	3.2	1.1	0.06	0.07	0.15
1440	388	396	401	0.002	-	-	-	-	-	-
6000	414	427	427	<0.001	-	-	-	-	-	-
59000	386	406	406	<0.001	-	-	-	-	-	-
DOUBLE AGEING AT 180°C										
0h	388	396	401	0.002	-	-	-	-	-	-
2	309	316	358	0.046	13.5	2.8	-	0.05	0.04	-
4	246	251	308	0.093	10	2.2	0.9	0.04	0.05	0.13
8	230	236	296	0.076	9	1.9	0.7	0.03	0.05	0.11
12	211	215	281	0.082	6.1	-	0.9	0.02	0.02	0.15

* Plastic strain corresponding to maximum true stress

homogeneous, a precipitate free zone 20 - 30nm wide was observed at grain boundaries, Fig 3(b). Prolonged aging at 120°C increased the precipitate size to ∿5-9nm and decreased precipitate density to $\sim 5 \times 10^{16}$-$10^{17} cm^{-3}$.

Double aging at 180°C coarsened the precipitate distribution and increased the precipitate free zone width to ∿0.2μm. The precipitates had a more rod-shaped morphology, 10 - 15nm in diameter and 20 - 40nm long and their density was $\sim 10^{16} cm^{-3}$. Transmission electron microscopy of deformed samples revealed that in the solution treated state dislocations had interacted to form a cell-structure, Fig 4(a). Natural aging and aging for short times at 120°C seemed to have relatively little effect upon the dislocation distribution in specimens strained to fracture. A very marked change in dislocation structure was observed when specimens were aged for 24h or more, Fig 4(b). In this state, intensely deformed bands were observed with the material between the bands being dislocation free. The bands were up to a few microns in width and extended across the entire width of a grain. Typically, the bands appeared in groups, with only one or two groups of bands in each grain. The double aged at 180°C samples deformed homogeneously and no intense slip bands were observed. In our studies, little evidence of grain boundary sliding was observed.

2.3.3 Fractography

Optical and scanning electron microscopy have been used to characterize the fracture mode. Two fracture modes were found:

1. Ductile shear failure, Fig. 5(a), in quenched, natural/under-aged and double aged samples.
2. Intergranular fracture, Fig. 5(b), in peak-aged samples.

2.3.4 Acoustic Emission

The acoustic emission activity of individual specimens is a strong function of plastic strain whilst the specimen to specimen emission is very dependent upon heat treatment.

The variation of acoustic emission power (rate) and stress with specimen extension is shown in Fig 6, for samples in the quenched condition and three naturally aged states. Three effects were noted in the emission of quenched material:

- the generation of a peak in acoustic emission just after general yield, Fig 6(a). The peak was composed of many overlapping events of wide amplitude range. Because of the relatively slow response of the chart recorder pen ($\sim$0.1s) these tend to be recorded in integrated form.
- Small periodic increases in acoustic emission power during post yield deformation linked to the occurrence of serrated yielding (not visible in Fig 6).
- A few (20-30) large amplitude signals, randomly generated throughout deformation and unrelated to serrated yielding events.

Natural aging had three effects upon the emission power - extension relation:

- The yield region emission peak disappeared to be replaced by a few isolated, individually energetic, burst signals.
- Serrated yielding and its associated emission gradually disappeared with aging.
- During plastic deformation increasing numbers of burst emissions were generated in aged samples.

Aging at 120°C resulted in similar, but more pronounced changes in the emission dependence upon extension, Fig 7. Prolonged aging resulted in disappearance of the yield region peak and the generation of individually energetic burst signals. These increased both in magnitude and frequency of occurrence as peak hardness was approached.

The effects of a second aging treatment at 180°C. Fig 8, were:

- The reappearance of a yield region peak in acoustic emission power similar but located at a smaller plastic strain, to that observed in the quenched sample.

. The rapid loss of energetic burst signals during plastic deformation.

2.4 Discussion

The variations in acoustic emission activity during deformation and the influence of heat treatment are, we believe, a consequence of changes in mode of deformation with some modes generating more energetic signals than others. Previous studies [4,5] have shown that for deformation by slip, the emission signals are dominated by a longitudinal pulse, Fig 9, and the displacement amplitude of this pulse is given by:

$$u_3 = \frac{c_2^2 bav}{c_1^3 x_3}$$

where c_1 is the longitudinal wavespeed, c_2 is the shear wave speed, b is the dislocation Burgers vector, a the distance of dislocation propagation, v the dislocation velocity and x_3 the source-to-detector distance. Inserting values of $c_1 = 6.4 mm\mu s^{-1}$, $c_2 = 3.2 mm\mu s^{-1}$, $b = 2.9 \times 10^{-10} m$ and $x_3 \sim 40mm$ we get, for aluminum:

$$u = (2.8 \times 10^{-13} sm^{-1})av$$

Thus a single dislocation moving at a velocity of $200 ms^{-1}$ would give a displacement of $10^{-14} m$ if it moved a distance of $\sim 200 \mu m$. Such a signal is considered on the limit of detection with existing instrumentation. Thus, only dislocation motions for which the product av exceeds a critical value ($\sim 4 \times 10^{-2} ms^{-1}$) are likely to generate detectable signals.

2.4.1 Naturally Aged Samples

Initial yielding of quenched material generated significant levels of continuous type acoustic emission. This was probably emitted by dislocations that escaped from solute atmospheres or clusters formed either during quenching or the brief period at room temperature prior to or during testing, Fig 10. Since in the initial stage of deformation the mobile dislocation density is likely to be low, some free dislocations would move at high speed ($\gtrsim 1200 ms^{-1}$ say) to satisfy the imposed rate of straining. Furthermore, the initially low dislocation

density results in relatively few barriers to slip so enabling moving dislocations to propagate distances comparable to the grain size (420μm). This type of deformation event has an av product of $\sim 8 \times 10^{-12} m^2 s^{-1}$ and would thus emit only a barely detectable signal. Only if many such events were simultaneously occurring throughout the specimen would this then give rise to an emission of the form observed. The decrease in emission with strain is presumably linked to an exhaustion of suitably pinned dislocations and the development of an internal dislocation structure which restricts the distance moved by individual dislocations.

After large deformations, when the dislocation density was high (dislocation velocity low), dynamic strain aging developed and this generated continuous emission during load drops. The high dislocation density severely restricts the distance individual dislocations moved; thus many dislocations must have cooperatively escaped their solute pinning allowing momentarily, deformation to occur at lower load and a detectable acoustic emission signal to be generated.

A few, randomly occurring signals were observed during the testing of quenched material. This seemed unconnected with load drops on the stress-strain curve and leads us to consider it unconnected with dynamic strain aging. One possible mechanism could be the unpinning of dislocations from fine precipitates formed during the test. Escape from these would probably require high local stresses which in turn would drive escaped dislocations at high speed causing generation of large amplitude signals.

Natural aging resulted in the continuous emission at yield being replaced by variably energetic burst signals. This could have arisen through an increase in pinning point strength due to heterogeneous precipitation upon dislocations. This would reduce the number of escape events and thus the density of highly mobile dislocations. This could lead to fewer, but more energetic emission generation events.

2.4.2 120°C Aging

In both long naturally aged samples and samples aged at 120°C toward peak

strength very energetic bursts of acoustic emission were observed. The effect increased as peak strength was approached and correlated with the appearance of intense local slip bands[6]. These bands are thought to occur in an unstable manner due to precipitate shearing, Fig 11, and we consider them to be the most probable source of the emission. Such a source consists of the rapid propagation of hundreds or even thousands of dislocations over distances comparable to the grain size. Thus, the sum $\sum a_i v_i$ of all the i dislocations involved is likely to be very large and could account for the energetic quality of this emission. A second contribution to the emission could have been the formation of intergranular microcracks; these may have been more important toward the end of each test.

2.4.3 Double Aging at 180°C

Double aging suppressed both intense slip band formation and energetic burst emission (the few signals in 2 and 4h aged material after large plastic strains, may have been due to slip band localization under a very high local stress). Double aging did however result in the appearance of a broad continuous emission peak at yield.

The appearance of the continuous emission is at first sight surprising since the closely spaced precipitates are effective barriers to propagating dislocations and would limit propagation distances to the order of the interparticle spacing ($\lambda p \sim 0.2\mu m$), Fig 12. Unrealistically large numbers of dislocations would then be required to give a detectable signal. However, if we consider the case of a large dislocation loop (radius r) suddenly "shuffling" from one set of precipitates to the next so that its radius became $r + \lambda p$ then for sufficiently large an r sufficient area might be swept out to emit a detectable signal, Fig. 13.

For example, if $r = 50\mu m$ and $\lambda p \sim 0.1\mu m$ then the area of slip is $\sim 30\mu m^2$. This, for a velocity of $10^3 ms^{-1}$ would result in a displacement of $\sim 8 \times 10^{-16} m$, so that 10 to 100 simultaneous loop shuffles would be required to give a detectable signal. The number of required loops decreases with λp; a $10\mu m$ interparticle spacing would need only a single loop shuffle. Thus we would expect an increase in emission with

aging time and this, indeed, is precisely the observed trend.

In summary, Al 5.5 Zn 2.5 Mg generates emission that is highly dependent upon heat treatment because of the strong effect upon deformation behavior. Material in the peak hardened condition generates the largest amplitude signals and this seems to be related to the occurrence of coarse slip band formation. Such processes are important in the nucleation of fatigue cracks in certain classes of aluminum alloys indicating the possibility of a very early indication of fatigue cracking problems.

3. Quantitative Acoustic Emission Source Characterization in Compact Tension Specimens

3.1 Introduction

The aim here is to establish a basis for the use of acoustic emission as a quantitative NDE technique, so that it can be applied with confidence to the monitoring of structural integrity. Experience from field application has clearly shown that commercial acoustic emission techniques are not yet capable of reliable defect characterization or sizing and this is severely restricting the range of applications of the technique. We have been following a step-by-step approach to this problem. First, the emission from brittle microcracks was modelled for an ideal wave propagation geometry[7], then we designed instrumentation that could digitally record those parts of the signal that were of fundamental importance[8]. Next we developed a sample (the Yobell) whose geometry, to a good approximation, was like a half-space so that we could apply our theory to experimental results[9]. We then set up a series of brittle and quasi-brittle microfracture sources and characterized these emission sources in terms of crack size and velocity[4,10] and found the characterization to be in good agreement with other, independent, estimates of the crack process. This demonstrated the feasibility of source characterization under ideal conditions.

In the work presented here we are moving on to examine the influence of the existence of a large precrack upon the emission from crack extension processes. We have tried to arrange for the crack extension process to be similar to one of the microcracking processes investigated earlier. The approach is to design a crack-growth geometry consistent with the need for psuedo half-space wave propagation and to measure acoustic emission waveforms at two orientations to the crack. The transducer and specimen transfer functions are deconvolved from these waveforms and a description of the source obtained.

3.2 Experimental

3.2.1 Specimen Design

The choice of specimen geometry was determined by the need to meet plane strain conditions of crack growth and yet to be able to use, to reasonable approximation, a half-space Greens' function for the transfer function. In order to meet the first requirement we adopted a compact tension design based upon BS5447, 1975, Fig 14. In order to satisfy the acoustic conditions it was required that no reflected signals arrive at the transducer locations (epicentres 1 and 2) before the direct shear arrival. Assuming at least a 1μs delay for a reflected wave to arrive after the direct shear wave leads to the following criteria upon specimen dimensions:

$$\left.\begin{aligned} &(A^2 + B^2)^{\frac{1}{2}}/c_1 > A/c_2 + 1\mu s \\ &(A^2+4H^2)^{\frac{1}{2}}/c_1 > A/c_2 + 1\mu s \end{aligned}\right\} \text{ for epicentre 1}$$

$$\left.\begin{aligned} &(4A^2+4h^2)^{\frac{1}{2}}/c_1 > H/c_2 + 1\mu s \\ &(B^2 + H^2)^{\frac{1}{2}}/c_1 > H/c_2 + 1\mu s \end{aligned}\right\} \text{ for epicentre 2}$$

A, B and H are defined in Fig 14 and c_1 and c_2 are the longitudinal and shear wavespeeds respectively.

It is not possible to simultaneously satisfy these criteria. It is possible to ensure plane strain conditions and no reflected arrival for epicentre 1 and this we chose to do. For epicentre 2, a side wall reflection will arrive before

the shear wave invalidating use of a half-space Greens' function beyond the reflection arrival time. This, it turns out, is not too serious since most of the analysis is based upon the longitudinal arrival. The dimensions of the specimen finally used are shown in Fig 15. They are similar to those of a standard 2" specimen, except the thickness is increased to 40mm which is permissible under BS5447.

3.2.2 Sample Preparation

A commercial medium carbon steel (BS4360, Grade 43A) of nominally identical composition to that of an earlier study with Yobell specimens was used. Samples were prepared with the rolling direction perpendicular to the plane of crack growth. Specimens were austenitised at 850°C for one hour and quenched into ice brine. No quenching cracking was observed.

Each specimen was fatigue precracked ∿5mm at a load range of 4 to 38kN which required 80,000 cycles. The load range chosen was quite critical; too high a load resulted in several catastrophic fractures.

3.2.3 Acoustic Emission Measurements

Four specimens were tested in an Instron 1195 machine at a crosshead rate of 0.2mm min^{-1} until the load capacity of the load cell was reached (50kN). This was sufficient to generate acoustic emission but insufficient to cause appreciable macroscopic crack growth. For two of the tests, a capacitance transducer was positioned at epicentre 1 with an air gap (which controls sensivitity) of 3.17μm. For the other two tests the transducer was at epicentre 2 and the air gap was 3.2μm. The remainder of the instrumentation has been reported elsewhere[7].

3.3 Results

A typical load-displacement curve is shown in Fig 16, the first acoustic emissions occurred when the load exceeded the fatigue preload. The number of emissions varied from test to test, typically it was ∿20. Representative waveforms for epicentre 1 and epicentre 2 are shown in Fig 17.

Each waveform was analyzed by deconvolving the Greens' function from it to give a source strength (taking into account the different orientation and depth of the

two epicentres). The source strength has the units of crack volume and two examples are shown in Fig 18. The maximum crack volume and crack growing time (lifetime) were measured from the source functions and the mean values are tabulated for each sample in table 3.

TABLE 3 Summary of CTS acoustic emission data

Specimen	Epicentre	No. Emissions	Crack depth mm	Mean strength μm^3	Mean life time ns
SW 600	1	15	17	22,700	350
SW 603	1	19	16	36,900	590
SW 602	2	23	24	18,300	480
SW 605	2	30	24	22,200	480

The difference between the values for the two epicentres can best be appreciated by comparing histograms in Fig 19. It is seen that the greater sensitivity at epicentre 2 is the cause for a smaller mean source strength. If this is accounted for there is little difference in the histograms.

Fractography indicated that loading caused only a small advance of the crack front centre ($\sim$1mm). The fracture mode consisted of isolated cleavage facets linked by ductile tearing.

3.4 Discussion

The simplest crack growth source to consider is a circular elastic microcrack[7] under mode I loading. This can be represented as a combination of force dipoles.

$$D_{ij} = C_{ijkl} b_k \delta A_l$$

where D_{ij} represents a product of two forces in the $\pm x_i$ directions with a separation in the x_j direction, b_k is a crack opening in direction x_k and δA_l the area of crack normal to direction x_l.

For the case of a horizontal crack (in the x_1 x_2 plane) we find

$$D_{ij} = \begin{bmatrix} 1.15 & 0 & 0 \\ 0 & 1.15 & 0 \\ 0 & 0 & 2.81 \end{bmatrix} \times 10^{11} b\delta A \text{ (Nm)}$$

It is instructive to calculate the directivity of the longitudinal wave amplitude for this source model. This can be done by resolving the tensor components D_{ij} along angle θ. In the far field the directivity

$$L(\theta) = \cos^2\theta + \frac{\lambda}{\lambda+2\mu} \sin^2\theta$$

$$= \cos^2\theta + 0.409 \sin^2\theta \text{ (for steel)}$$

This angular dependence is shown in Fig 20. The maximum amplitude occurs in the direction of maximum crack opening. The amplitude at 90° to this (epicentre 1) is reduced to 40%. The waveform at epicentres 1 and 2 can be found by combining the representation for the source with the appropriate components of the half-space Greens' function[11], and these are shown in Fig 21. We see that comparison with measured waveforms is reasonable, the measured waveforms tend to have broader arrivals. The more rapid droop of measured signals is due to high pass filtering at 30kHz.

The broadening of the waveform seems to be linked to the presence of the precrack and results in an increased apparent source volume by a factor of 10 compared with a similar source in Yobell specimens[4,10]. This broadening could be related to the relaxation/reverberation of the precrack in response to dynamic extension at the tip (this is consistent with previous work on notched Yobells of mild steel[7] which showed the effect of the notch was to widen the longitudinal pulse to make the source volume 2-3 times apparently larger).

Modelling exactly the dynamic response of the precrack to crack tip extension is a difficult problem. In the meantime, it is useful to consider a more simple model as follows:

Suppose we have a semi-infinite, planar elastic crack in an infinite body, Fig 22. The cross-section of the crack is parabolic, so the crack opening, y, is given as a function of position along the crack x, by [12]

$$y = \frac{4K_I(1-\nu^2)}{E}\sqrt{\frac{x}{2\pi}}$$

where K_I is the static stress intensity factor.

The volume per unit thickness of this crack, up to some length A, is then

$$V = \int_0^A \frac{8K_I(1-\nu^2)}{\sqrt{2\pi}\,E}\sqrt{x}\,dx$$

Now let the crack tip extend horizontally at a velocity v so that the increased length at time t is x=vt. We assume that the precrack relaxes to its parabolic profile, as in the static case, but that the region of relaxation propagated along at velocity c_2. The distance of relaxation is thus

$$x' = (c_2+v)t$$

The increase in volume per unit thickness at time t, until the crack is arrested at time t = a/v (where a is the distance of crack advance) is

$$\Delta V = \frac{8K_I(1-\nu^2)}{\sqrt{2\pi}\,E}\left[\int_0^{x'}\sqrt{x}\,dx - \int_0^{x'-x}\sqrt{x}\,dx\right]$$

$$= \frac{16K_I(1-\nu^2)}{3\sqrt{2\pi}\,E}\left[t^{\frac{3}{2}} \quad (c_2+v)^{\frac{3}{2}} - c_2^{\frac{3}{2}}\right] \qquad t < a/v$$

After the microcrack is arrested (at t = a/v) the only increase in crack volume is due to relaxation. Now

$$x' = c_2 t + a$$

Thus,

$$\Delta V = \frac{8K_I(1-\nu^2)}{\sqrt{\pi}\,E}\left[\int_0^{x'}\sqrt{x}\,dx - \int_0^{x'-a}\sqrt{x}\,dx\right]$$

$$= \frac{16K_I(1-\nu^2)}{3\sqrt{2\pi}\ E}\left[(c_2t+a)^{\frac{3}{2}} - (c_2t)^{\frac{3}{2}}\right] \quad t \geq a/v$$

For $t >> a/v$ this approximates to

$$\Delta V = \frac{8K_I(1-\nu^2)}{\sqrt{2\pi}\ E}\left[c_2^{\frac{1}{2}} + \right]$$

Using $a = 500ms^{-1}$ and $c_2 = 3240ms^{-1}$, $\Delta V(t)$ is shown in Fig 23. It can be seen that the relaxation of the precrack increases the source volume by a factor of 9 at the mean source lifetime of 500ns. Thus, this simple, quasi-static 2-d model seems able to account for the amplification of acoustic emission signals from precracked samples.

4. Conclusions

Systematic studies of the role of metallurgical variables are beginning to provide an understanding of the physical processes that generate detectable signals. In a pure Al 5.5 Zn 2.5 Mg alloy, the most dominant source seems to be the formation of intense slip bands linked to the shear of precipitates. This process is commonly incorporated in models of fatigue crack initiation in aluminum alloys used in aerospace applications and so these results would indicate some promise for acoustic emission detection of crack initiation/propagation.

Quantitative source characterization during incremental advance of a large crack looks to be a viable proposition provided the source-detector configuration is known. The most important effect seems to be an apparent amplification of the acoustic emission signal compared with that from an isolated microcrack. This makes signals more easy to detect and inversion inherently conservative.

Acknowledgements

We gratefully acknowledge funding for these studies from A.M.T.E. (Holton Heath) and RAE (Farnborough) through MOD Procurement Executive.

References

1. J.M. Carlyle, J. Acoust. Soc. Am., Suppl 1 68, 1980, 8104

2. H.N.G. Wadley, C.B. Scruby and J.H. Speake, Int Metals Reviews 2 1980 41

3. I. Kovacs, J. Lendvai, T. Ungar, G. Groma and J. Lakner, Acta Met 28 1980 1621

4. C.B. Scruby, H.N.G. Wadley and J.E. Sinclair, Metal Science, June 1981 241

5. C.B. Scruby, H.N.G. Wadley and J.E. Sinclair, Phil. Mag 1981 TO BE PUBLISHED

6. N. Ryum, Acta Met 17 1969 821

7. C.B. Scruby, H.N.G. Wadley and J.E. Sinclair, I. Mech. E., 1979 C38/79 London

8. C.B. Scruby and H.N.G. Wadley, J. Phys. D: Appl. Phys. 11 1978, 1487

9. C.B. Scruby, J.C. Collingwood and H.N.G. Wadley, J. Phys. D: Appl Phys 11 1978, 2359

10. H.N.G. Wadley, C.B. Scruby and G. Shrimpton, Acta Met 1981 29 399

11. J.E. Sinclair, J. Phys D: Apply Phys 12 1980 1309

12. J.F. Knott, Fundamentals of Fracture Mechanics, 1973, Butterworths

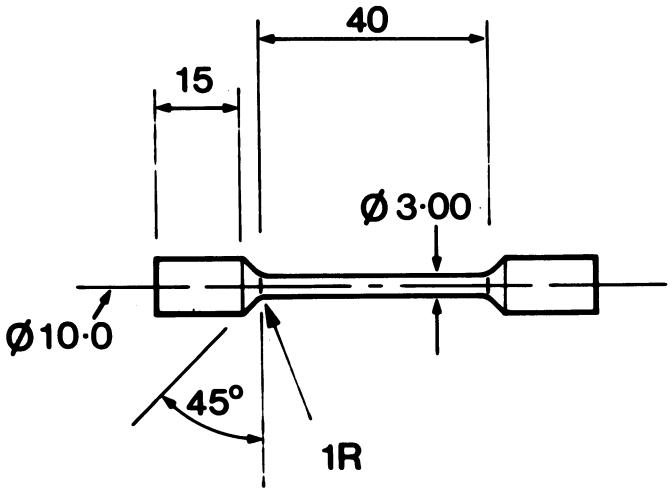

AERE - R 10258 Fig. 1
The dumbbell geometry used for uniaxial tensile tests from which narrow band acoustic emission activity was measured. The dimensions are given in millimetres.

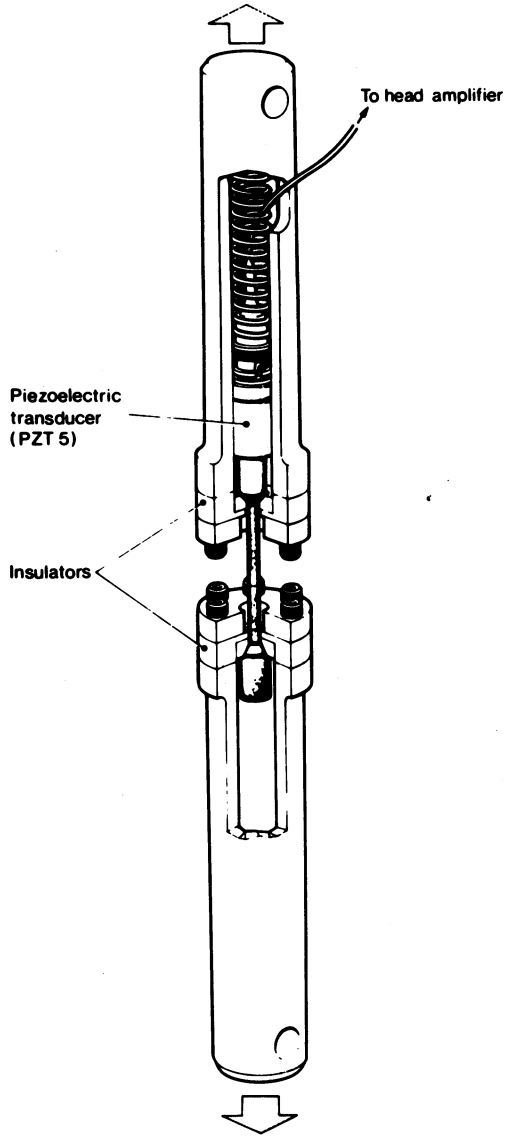

AERE - R 10258 Fig. 2
The gripping arrangement for uniaxial tensile testing of dumbbell specimens. The specimen and transducer were electrically insulated from the grips to improve signal to noise ratio.

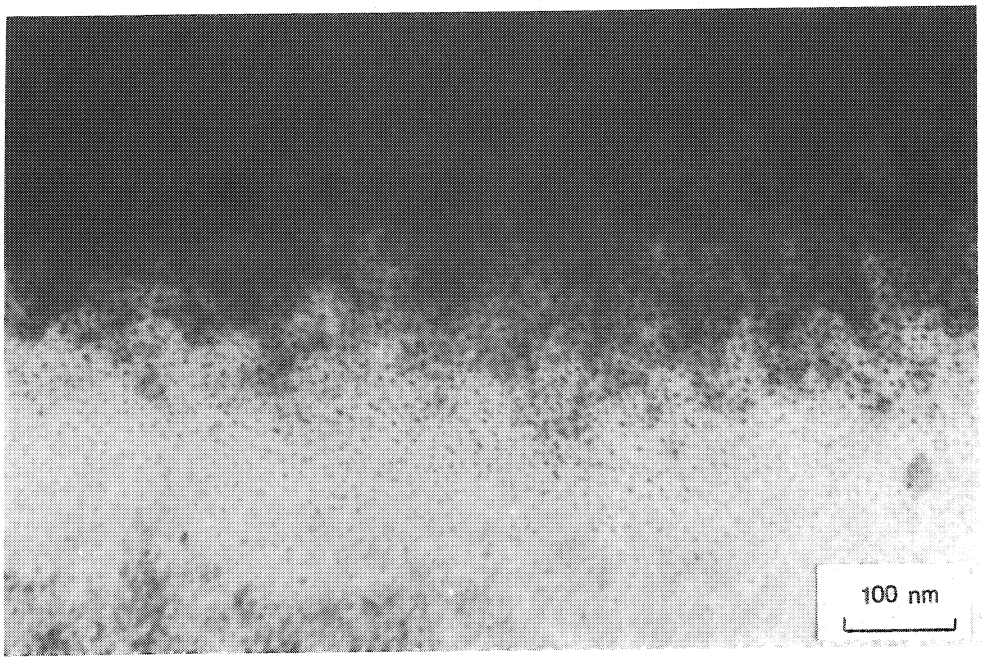

AERE - R 10258 Fig. 3(a)
Transmission electron micrograph of fine precipitates in alloy F68 aged at 120°C for 24h.

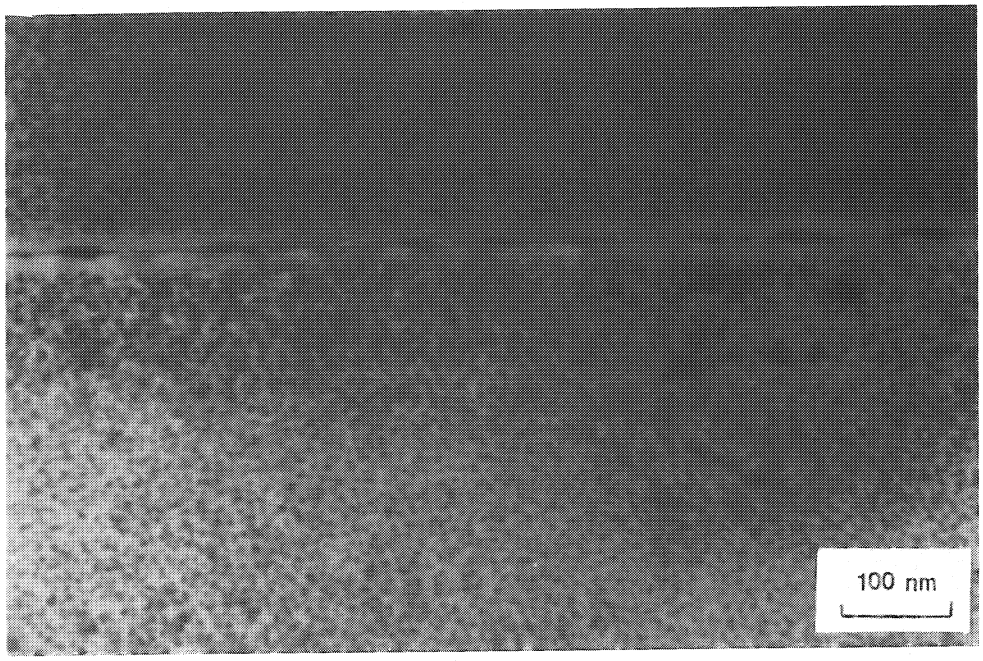

AERE - R 10258 Fig. 3(b)
Transmission electron micrograph of grain boundary region in alloy F68 aged at 120°C for 4d. The precipitate free zone and grain boundary precipitates are present.

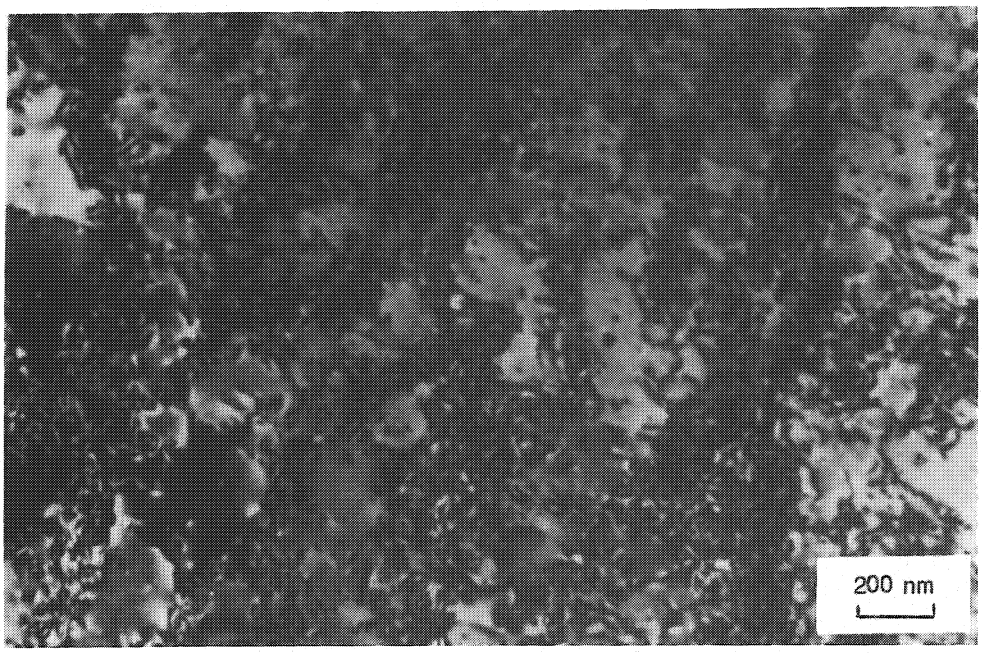

AERE - R 10258 Fig. 4(a)
Transmission electron micrograph of cell-like dislocation structure in alloy F68. As quenched.

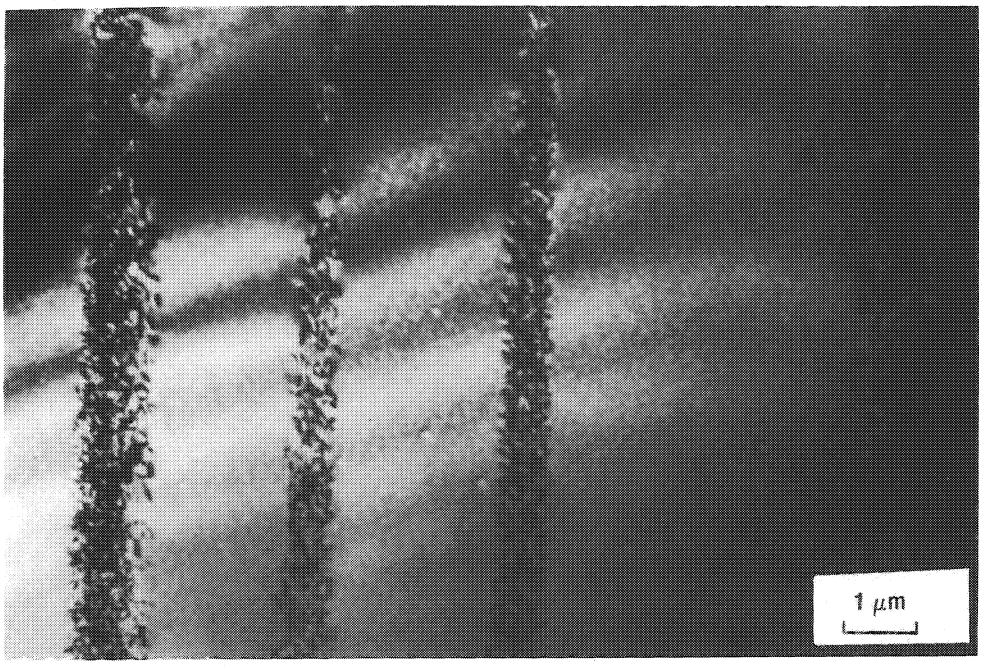

AERE - R 10258 Fig. 4(b)
Transmission electron micrograph of intense deformation bands in alloy F68 aged at 120°C for 24h.

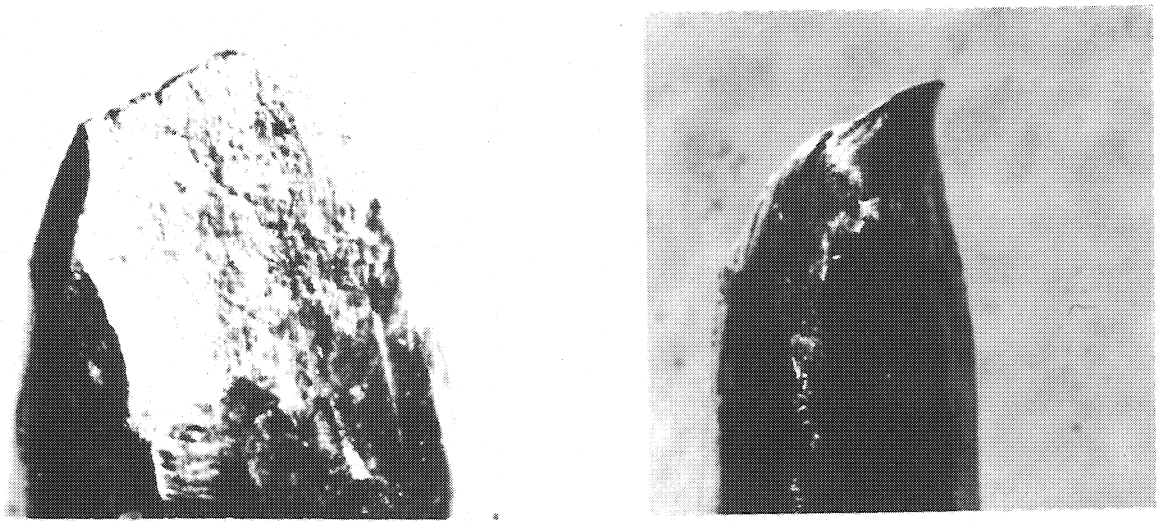

(I) (II)

AERE - R 10258 Fig. 5(a)
Optical micrographs of ductile fracture of alloy F68 aged at 120°C for 6m showing (I) fracture surface and (II) orientation of fracture surface and necking.

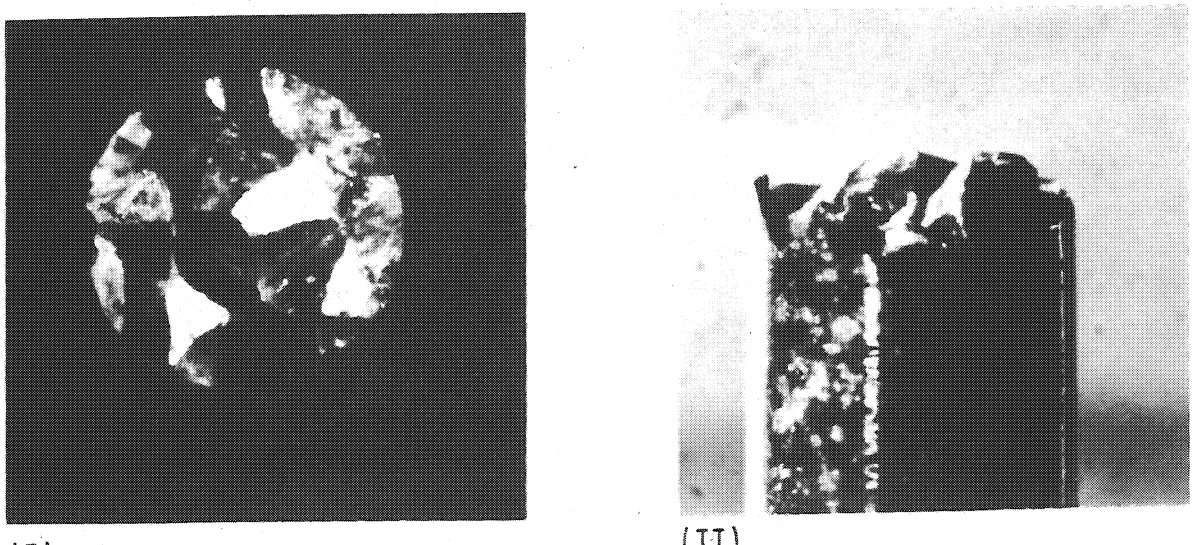

(I) (II)

AERE - R 10258 Fig. 5(b)
Optical micrographs of intergranular fracture of alloy F68 after peak ageing showing (I) fracture of surface and (II) orientation of fracture surface.

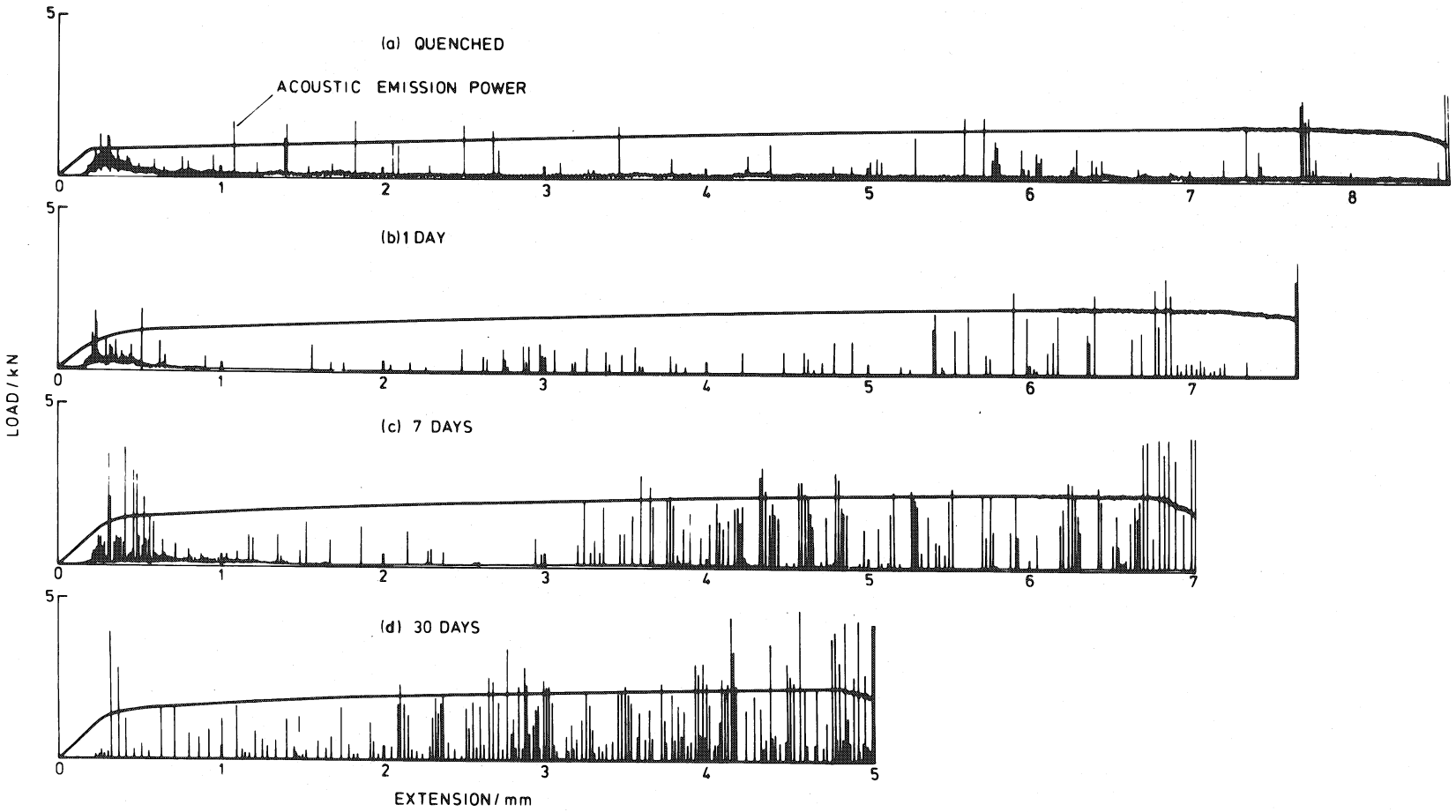

AERE - R 10258 Fig. 6
Effect of ageing at 20°C F68 material.

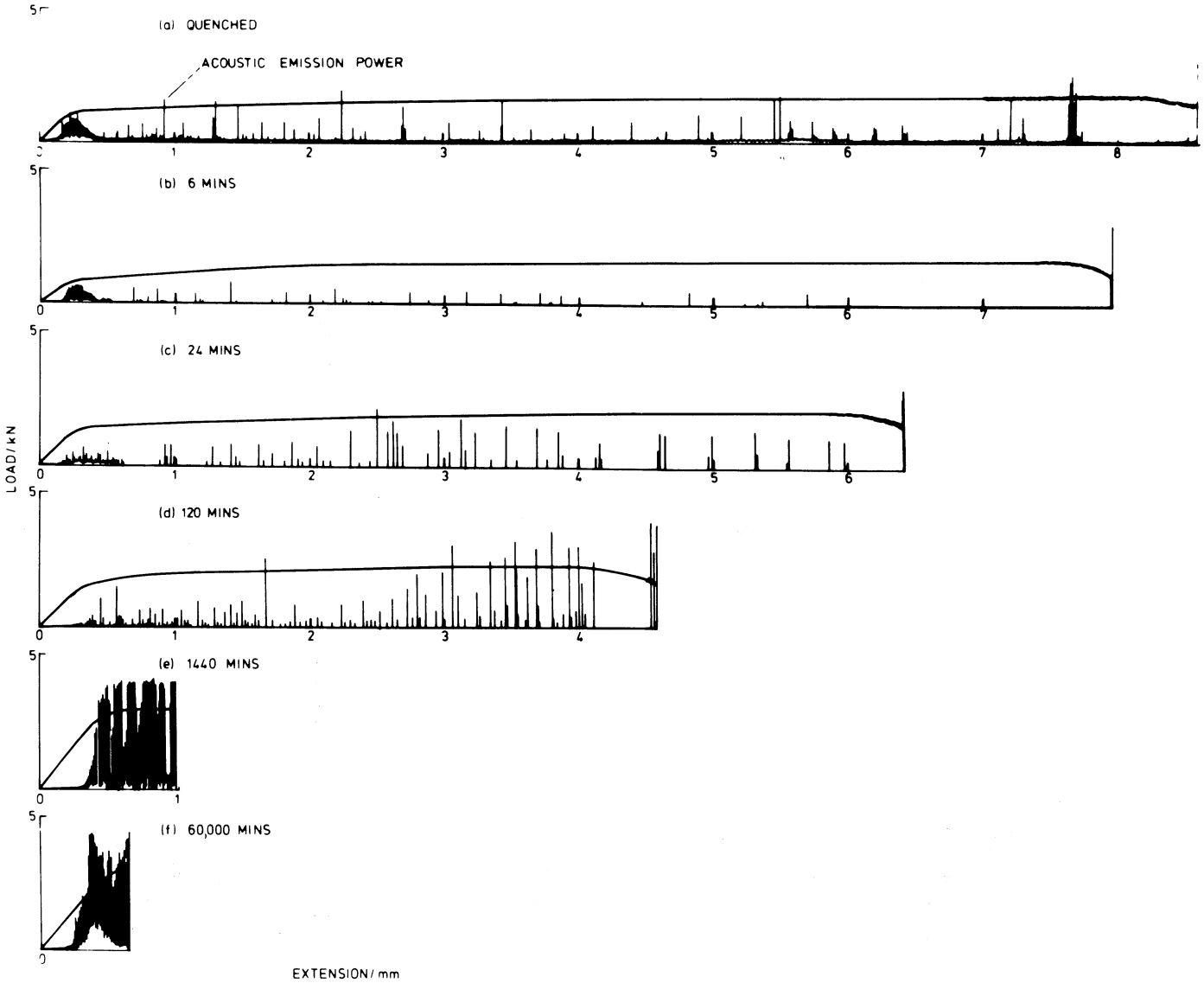

AERE - R 10258 Fig. 7
Effect of ageing at 120°C F68 material.

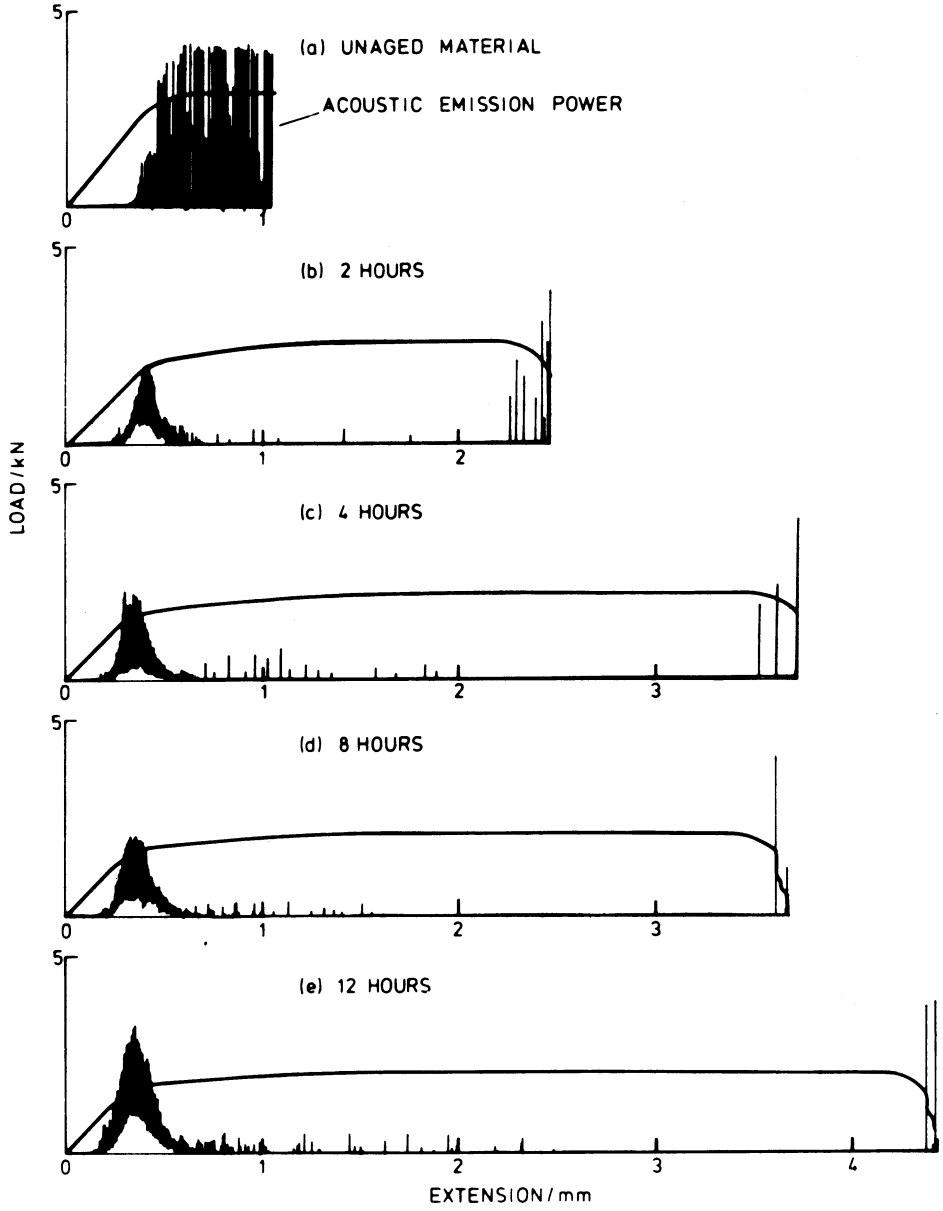

AERE - R 10258 Fig. 8
Effect of secondary ageing at 180°C F68 material.

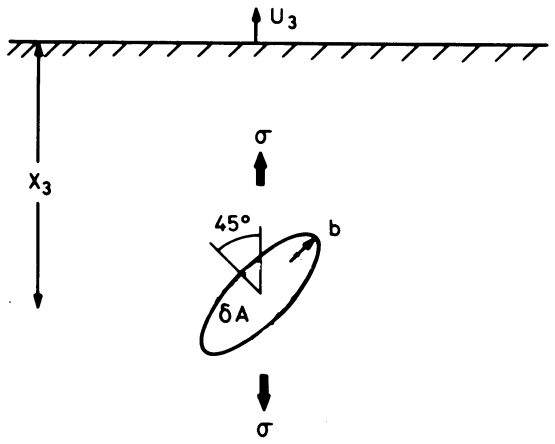

(a) DISLOCATION SOURCE INCLINED AT 45° TO STRESS AXIS, X_3

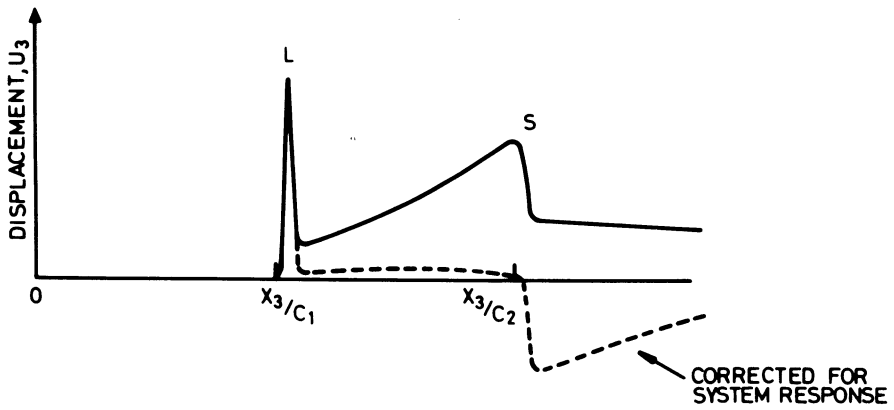

(b) EPICENTRE WAVEFORM FOR $b\delta A\ H(t)$ SOURCE FUNCTION

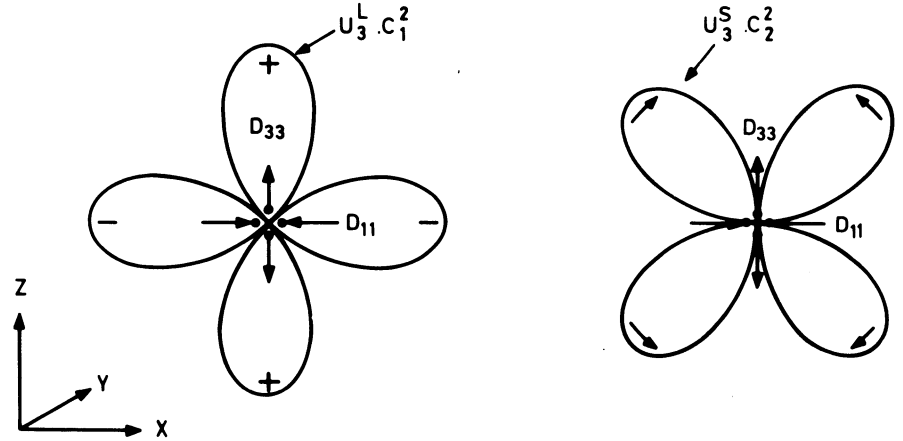

(c) ORIENTATION DEPENDENCE OF L AND S COMPONENTS

AERE - R 10258 Fig. 9

The model (a) used to evaluate epicentre surface displacements (b) from a dislocation source. (c) shows angular directivity of L and S waves emitted by (a).

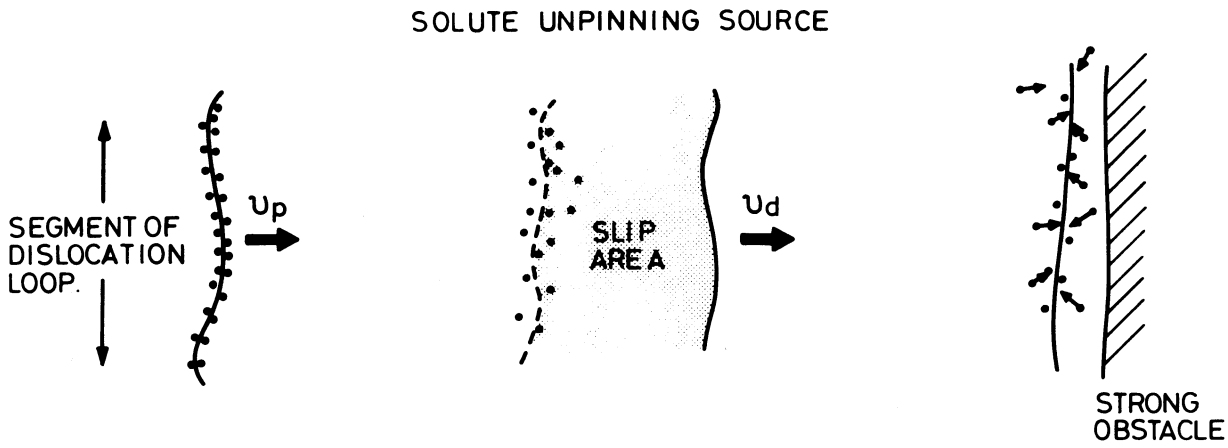

AERE - R 10258 Fig. 10

Schematic representation of solute pinning.

(a) Dislocation at t = 0 has an enhanced concentration of solute distributed around its core. Velocity v_p controlled by rate of diffusion of pinning species.

(b) If stress sufficiently high, dislocation breaks away and accelerates to velocity v_d typical of that stress and the matrix friction stress.

(c) Dislocation then hits an obstacle and is stopped. Solute then diffuses to dislocation.

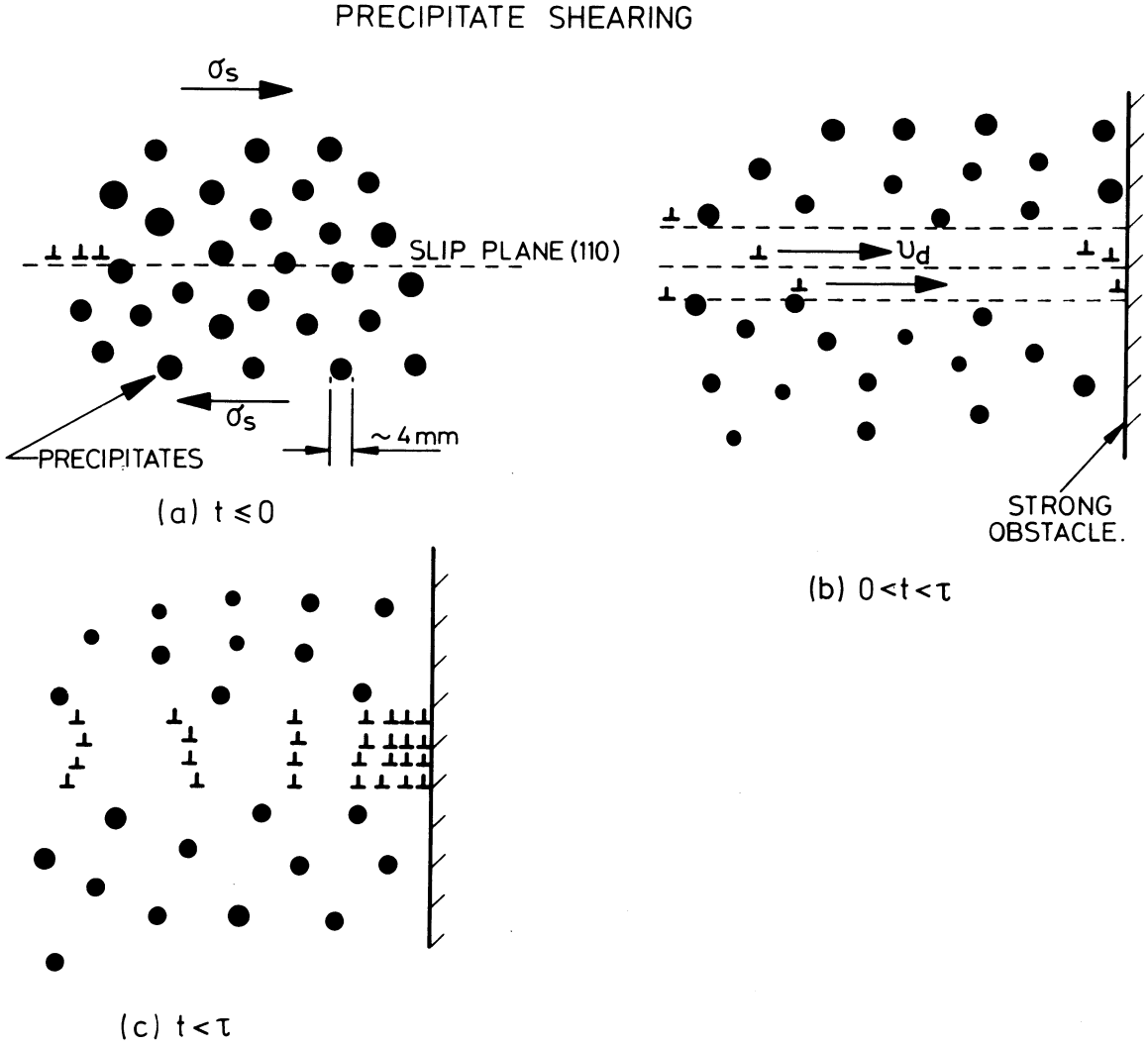

AERE - R 10258 Fig. 11

A schematic representation of a precipitate-shearing slip mode.

(a) Under the action of a high local stress (perhaps ahead of a dislocation pile-up) dislocations shear precipitates.

(b) Once sheared by several dislocations the precipitates dissolve, reducing the local flow stress.

(c) High speed dislocation motion occurs in the locally soft region until work hardening occurs.

OROWAN LOOPING OF PRECIPITATES

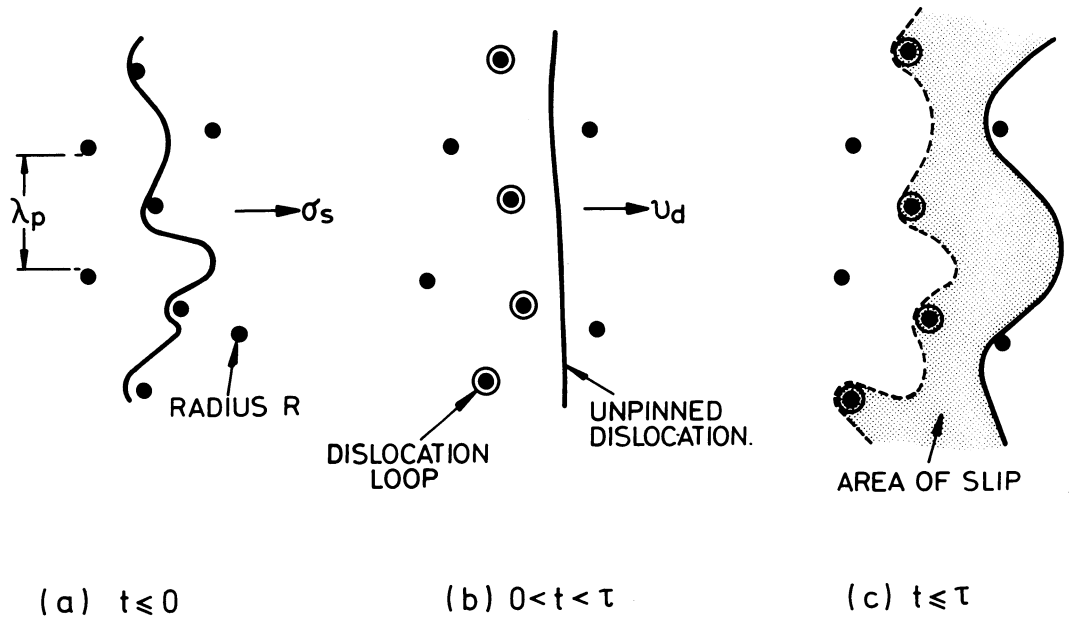

AERE - R 10258 Fig. 12

Schematic representation of Orowan looping around strong, widely spaced precipitates.

(a) Under action of shear stress σ_s, dislocation reversibly bows between particles.

(b) At a critical stress dislocation bypasses precipitate leaving a loop. Free segment of dislocation propagates at a velocity v_d.

(c) When dislocation reaches next strong precipitate it stops.

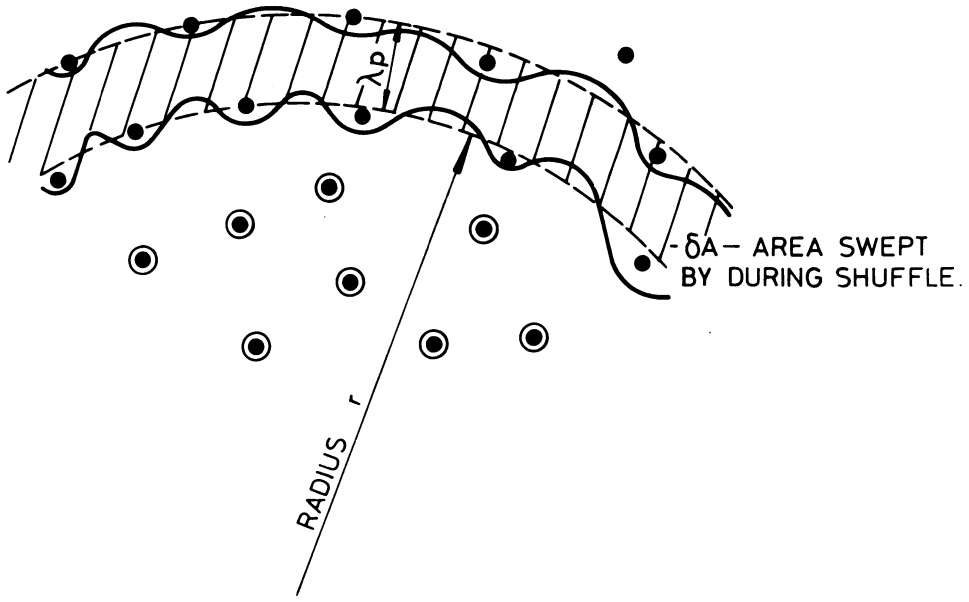

AERE - R 10258 Fig. 13

The "shuffle" of a loop of initial radius r out to the next set of dispersion hardening precipitates can generate a detectable signal for large r and λ_p.

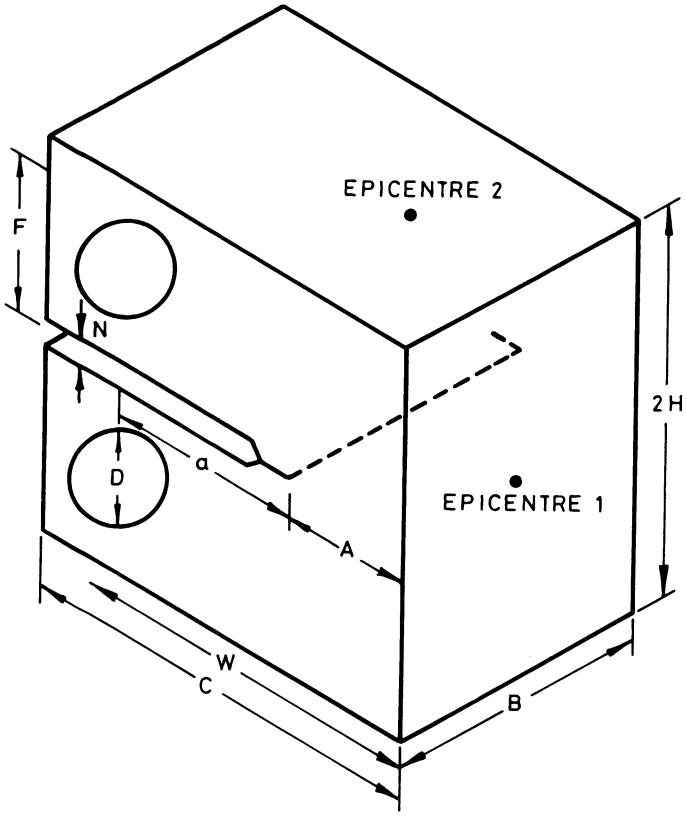

BS 5447 : 1977

NET WIDTH W	
TOTAL WIDTH C	= 1·25W
THICKNESS B	= 0·5W (OR IF REQUIRED 0·25W TO 1·25W)
HALF HEIGHT H	= 0·6W
HOLE DIAMETER D	= 0·25W
EFFECTIVE CRACK LENGTH a	= 0·45W TO 0·55W
NOTCH WIDTH N	= 0·065W MAX.
HALF DISTANCE BETWEEN HOLE OUTER EDGES F	= 1·6D

AERE - R 10258 Fig. 14
Showing compact tension specimen with dimensions referred to in the text.

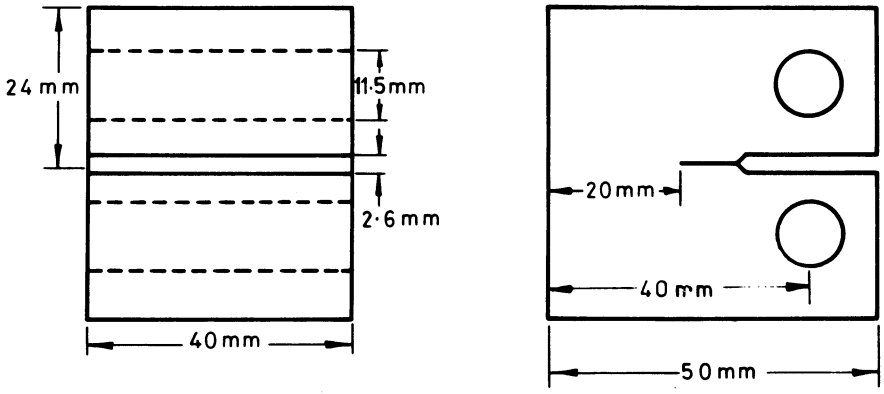

TO SCALE

AERE - R 10258 Fig. 15
CTS geometry satisfying mechanical testing and acoustic emission requirements.

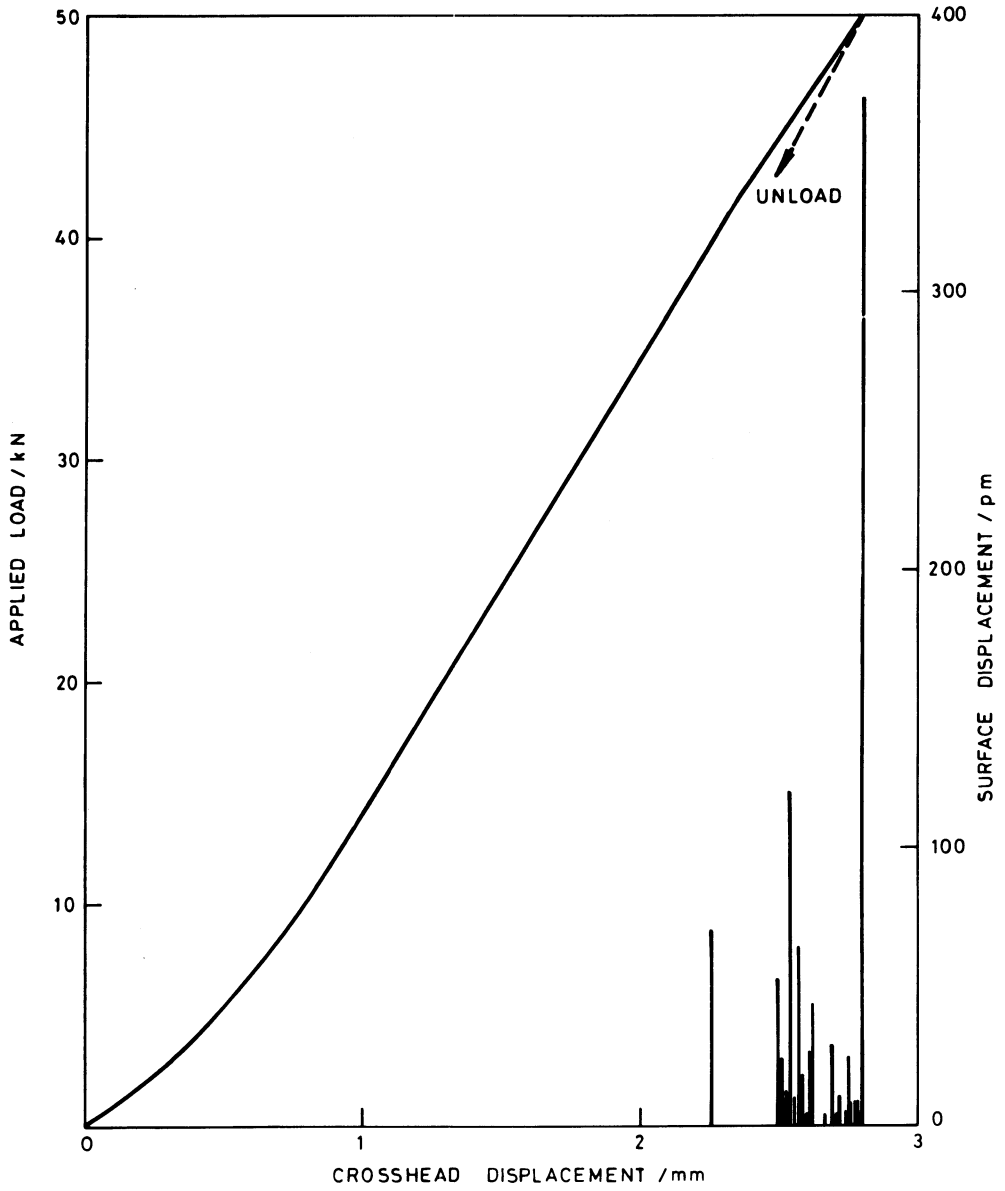

AERE - R 10258 Fig. 16

Applied load and acoustic emission amplitude as a function of crosshead displacement for CTS specimen SW 602. The specimen was unloaded before failure. All four specimens showed similar behaviour.

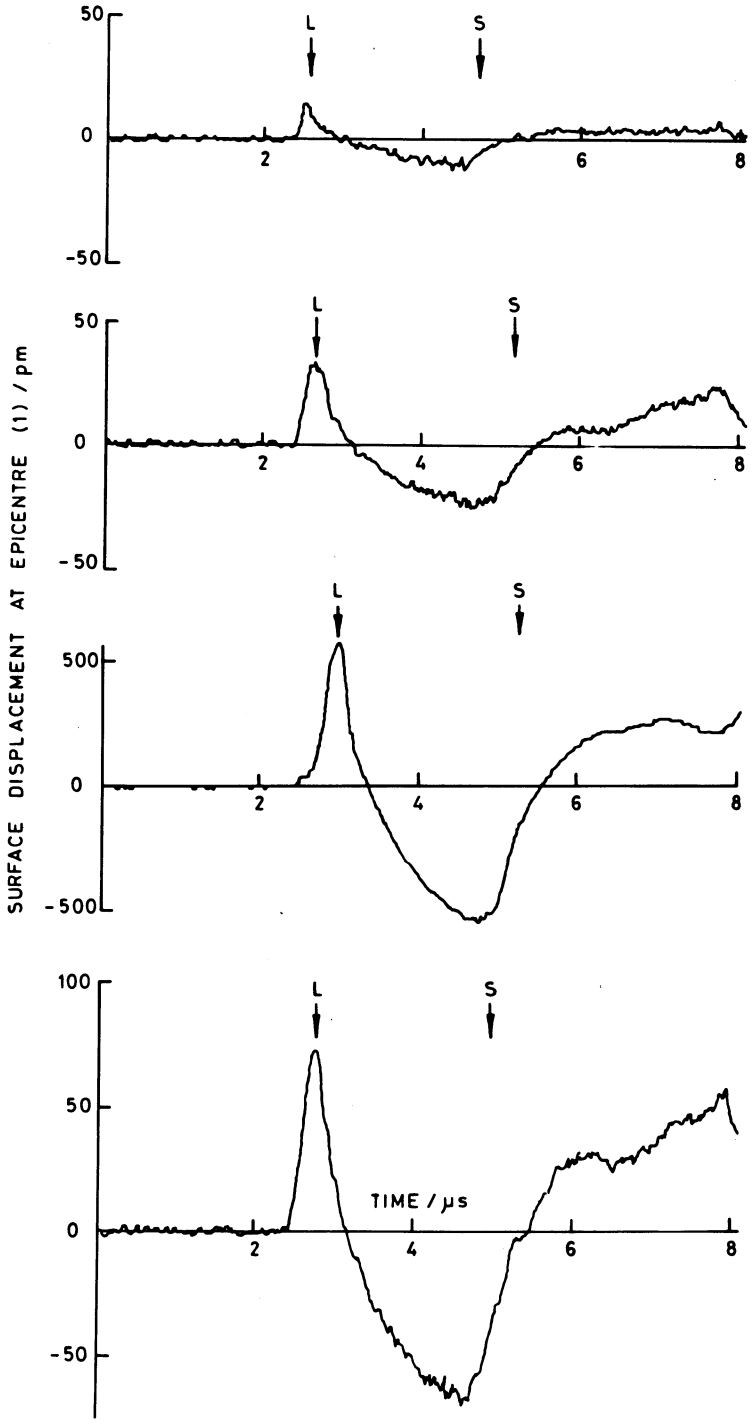

AERE - R 10258 Fig. 17(a)

Four typical emissions recorded at epicentre (1) from crack-growth in specimen SW 600. L and S are longitudinal and shear arrivals.

(Time origin arbitrary)

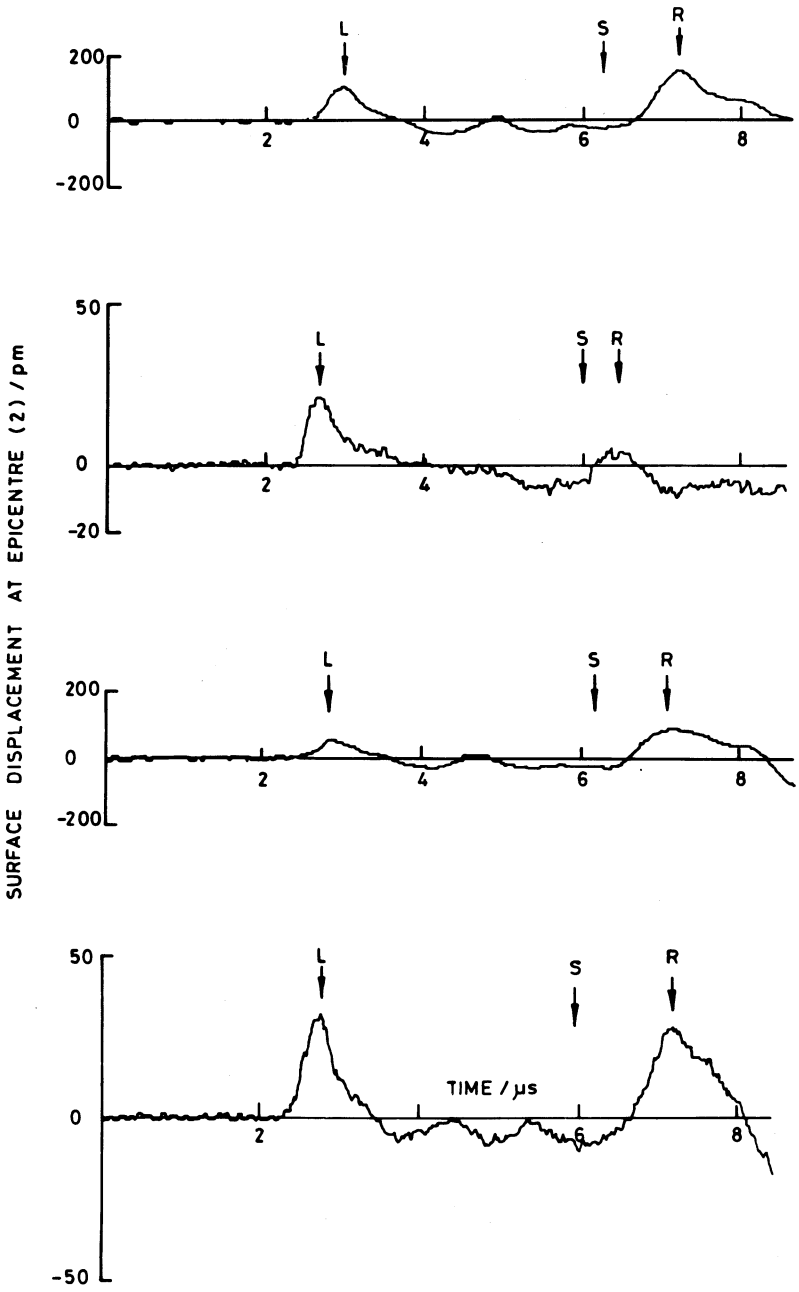

AERE - R 10258 Fig. 17(b)
Four typical emissions recorded at epicentre (2) from crack-growth in specimen SW 602. R is a side-wall reflection.

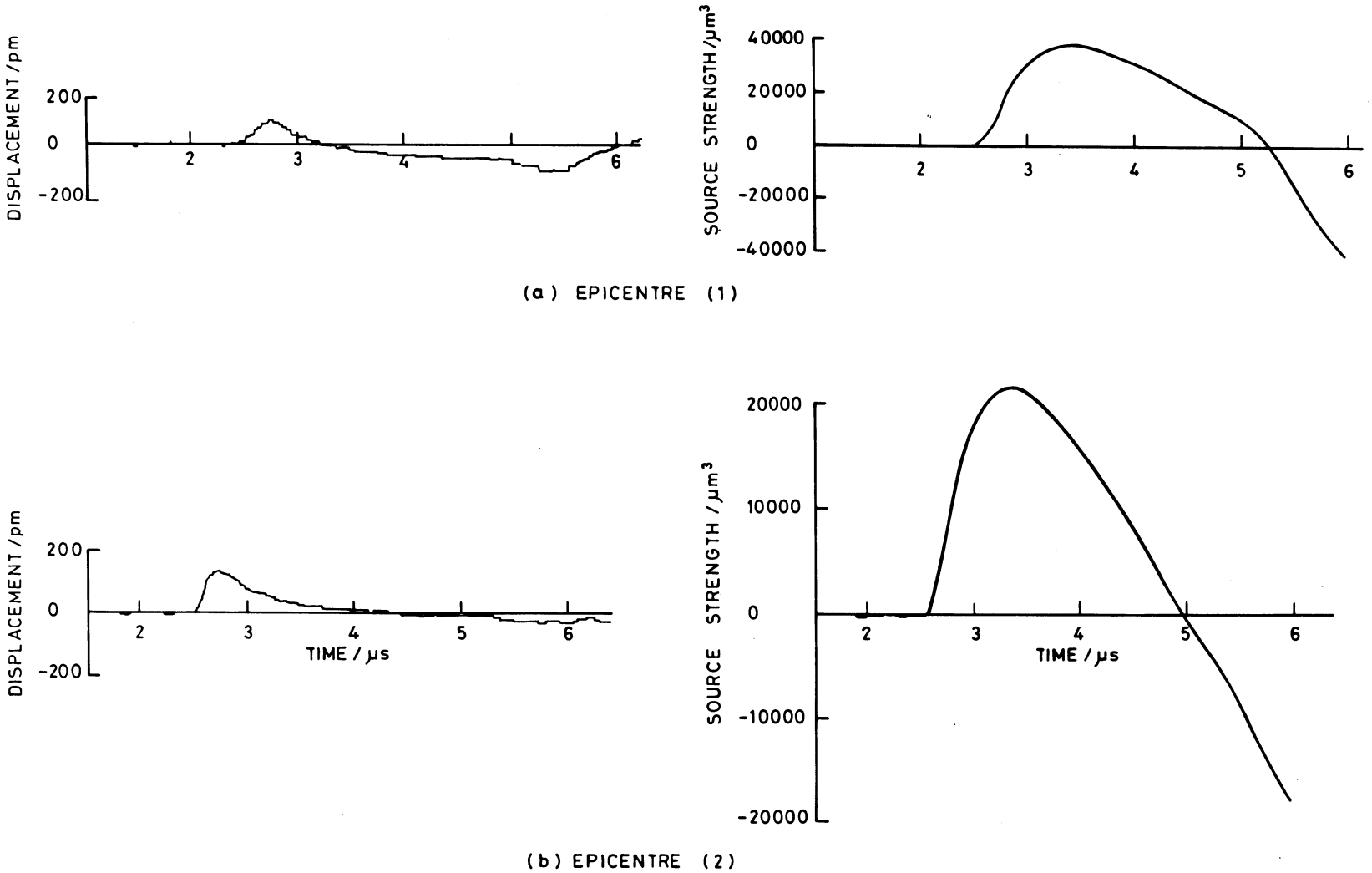

AERE - R 10258 Fig. 18

Showing source strength derived as a function of time by deconvolution of the $\frac{1}{2}$-space Green's function from acoustic emissions detected at both epicentres.

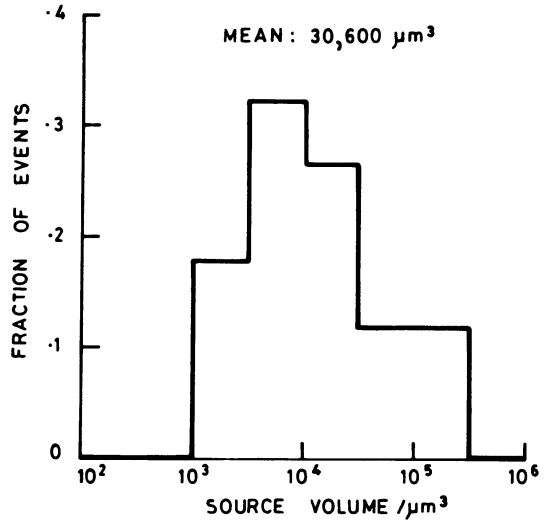

(a) EPICENTRE 1

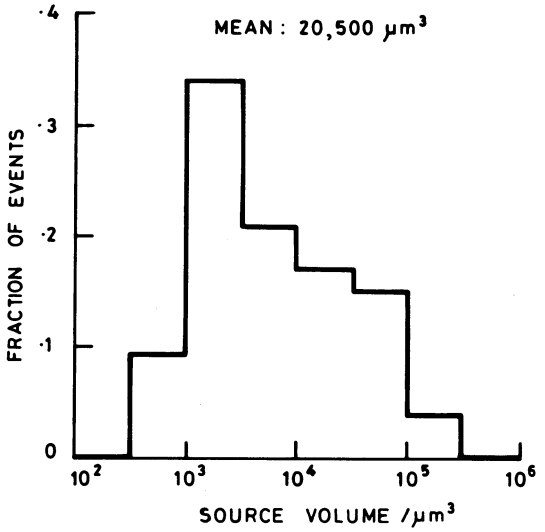

(b) EPICENTRE 2

AERE - R 10258 Fig. 19(a)
Histograms of source strength (volume) data for all the emissions recorded at each epicentre.

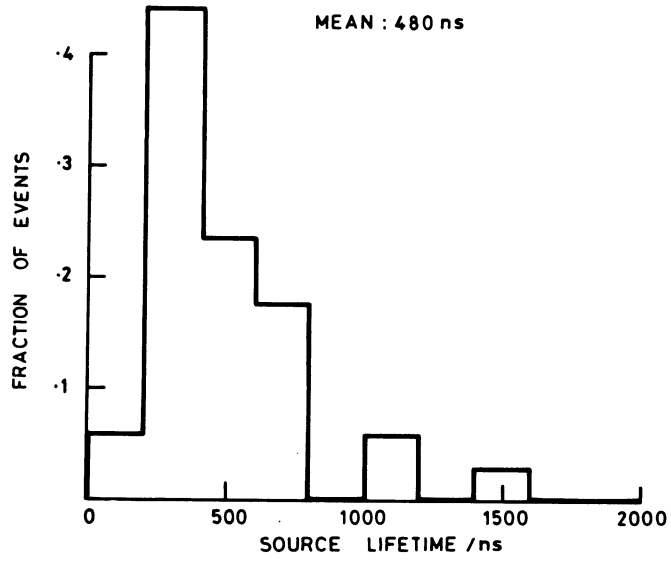

(a) EPICENTRE 1

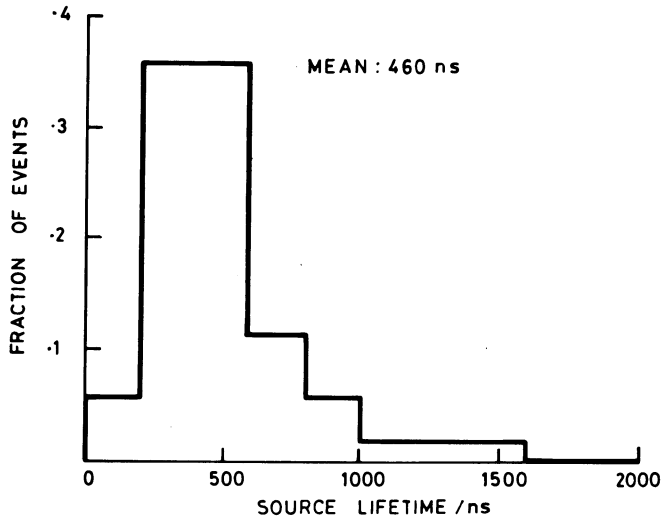

(b) EPICENTRE 2

AERE - R 10258 Fig. 19(b)
Histograms of source lifetime data for all the emissions recorded at each epicentre.

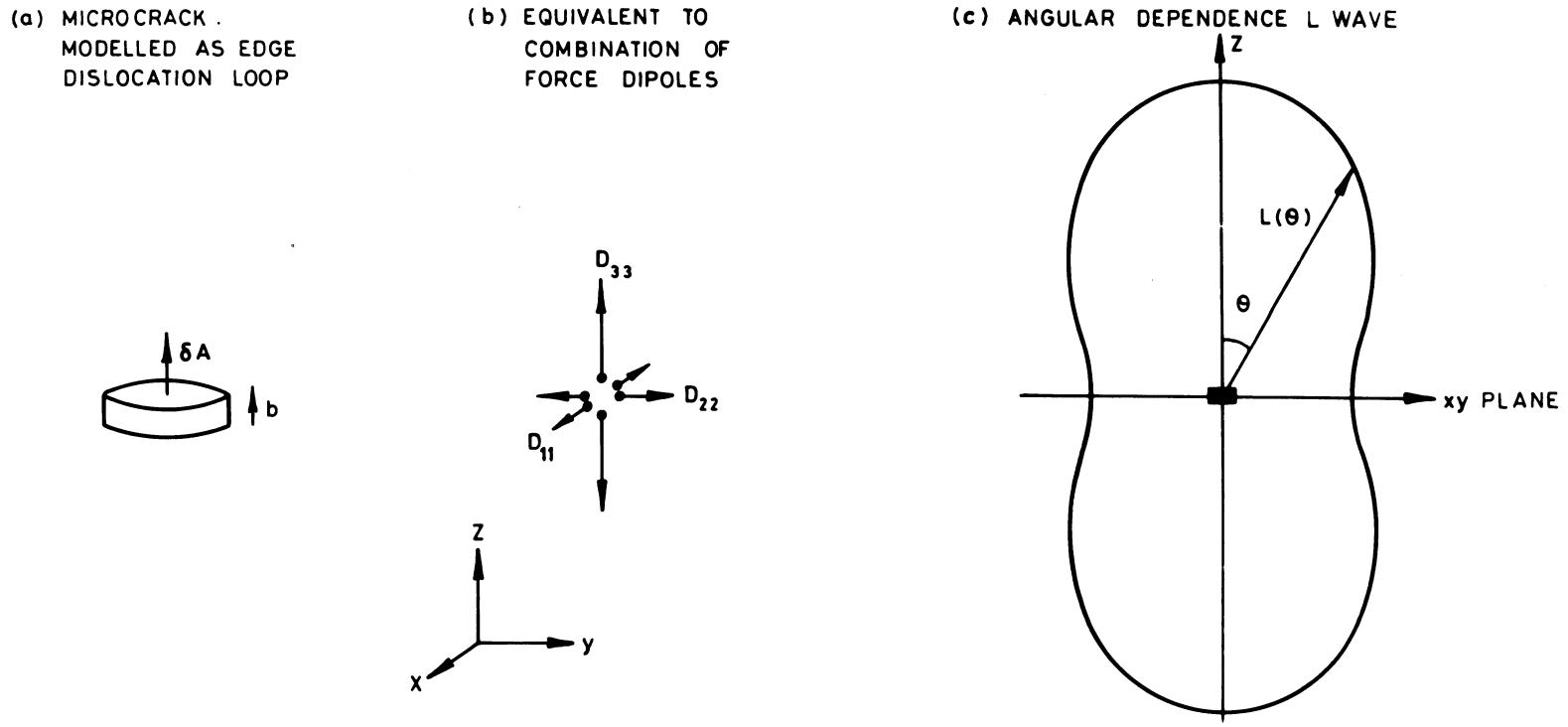

AERE - R 10258 Fig. 20

Microcrack is modelled as edge dislocation loop, which is equivalent to combination of 3 force dipoles, D_{ij}.

Angular dependence shows maximum parallel to z axis.

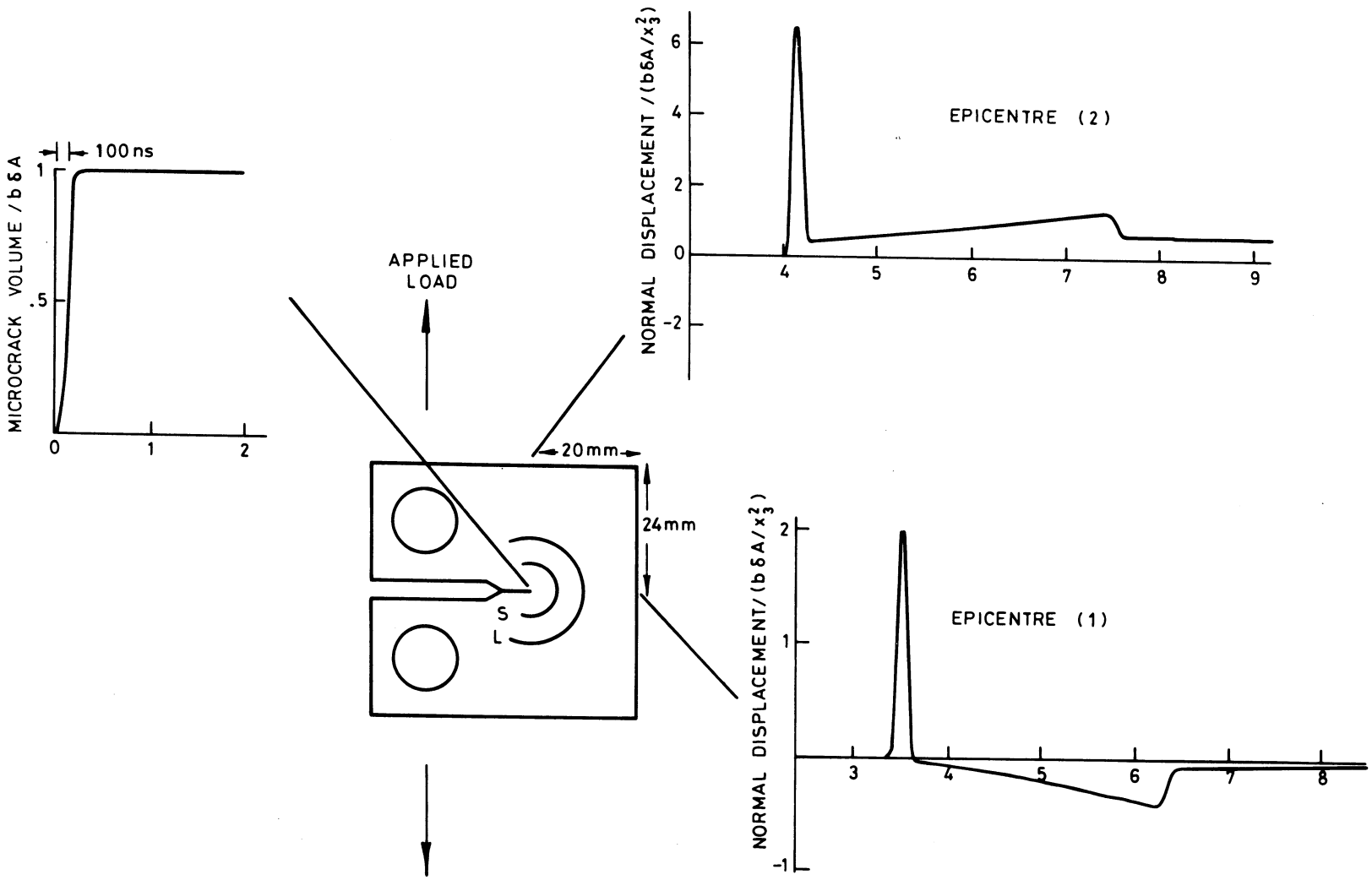

AERE - R 10258 Fig. 21

Displacement waveforms computed, assuming $\frac{1}{2}$-space solution, for two epicentres of CTS specimen in response to microcrack source at crack tip.

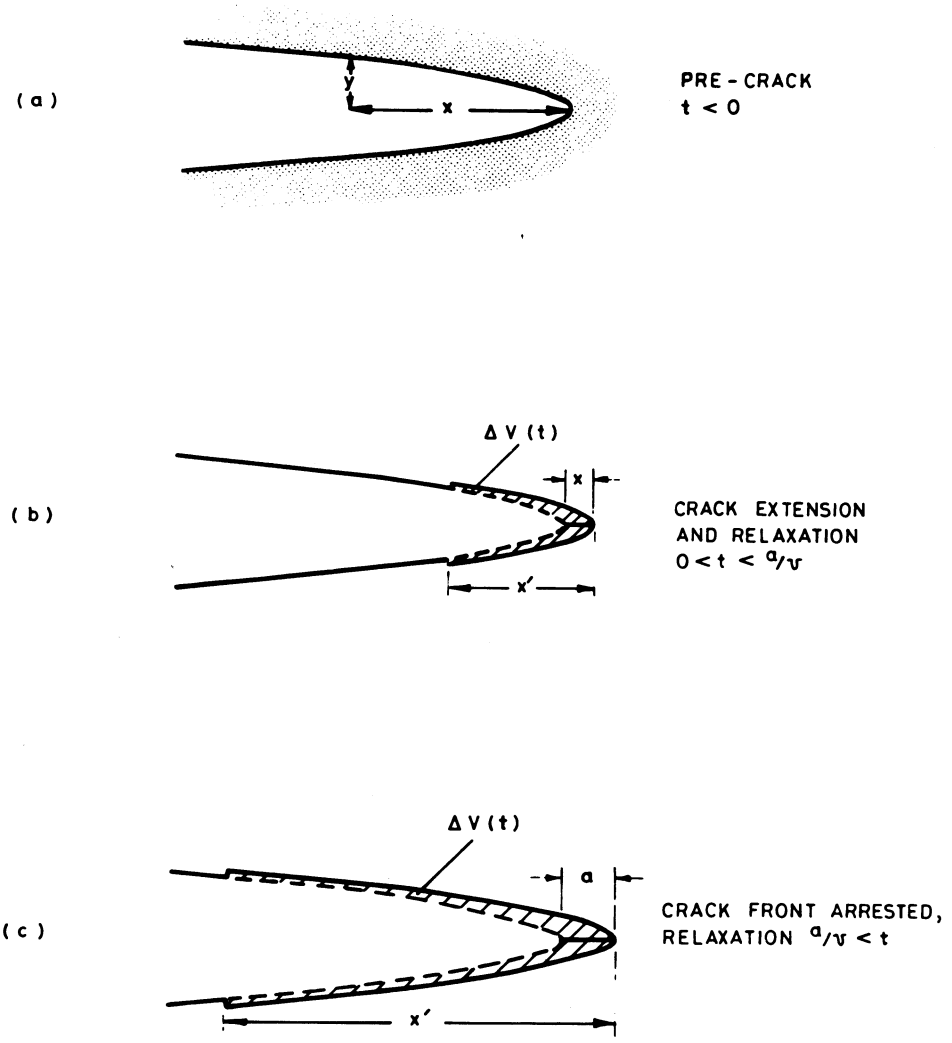

AERE - R 10258 Fig. 22

Simplified model for crack growth. (a) Pre-crack is parabolic in cross-section. (b) Crack tip advances at velocity v, pre-crack relaxation to equilibrium position propagates back at velocity c_2. (c) After crack-tip arrest (length a) precrack continues to relax until all at equilibrium.

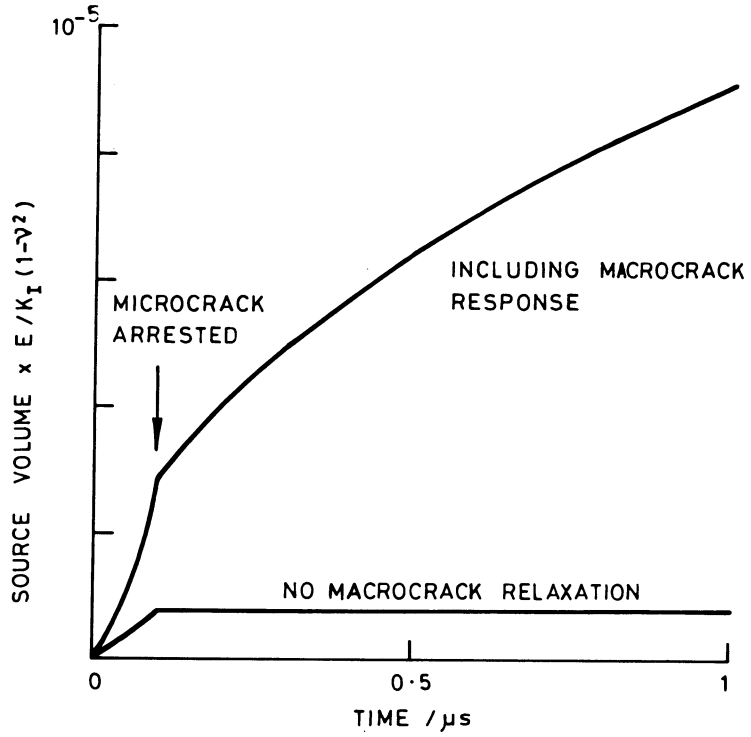

AERE - R 10258 Fig. 23

Source volume (per unit thickness) as function of time, based on model in Fig. 22. Volume also plotted neglecting pre-crack relaxation for comparison.